

## Review Article

# The NOMAD Experiment at CERN

**F. Vannucci**

*LPNHE/APC, Université Paris 7-Diderot, 4 place Jussieu, 75005 Paris, France*

Correspondence should be addressed to F. Vannucci; [vannucci@in2p3.fr](mailto:vannucci@in2p3.fr)

Received 19 June 2013; Revised 9 September 2013; Accepted 11 October 2013; Published 20 January 2014

Academic Editor: Leslie Camilleri

Copyright © 2014 F. Vannucci. This is an open access article distributed under the Creative Commons Attribution License, which permits unrestricted use, distribution, and reproduction in any medium, provided the original work is properly cited. The publication of this article was funded by SCOAP<sup>3</sup>.

The purpose of this paper is to review the experimental apparatus and some physics results from the NOMAD (neutrino oscillation magnetic detector) experiment which took data in the CERN wide-band neutrino beam from 1995 to 1998. It collected and reconstructed more than one million charged current (CC)  $\nu_\mu$  events with an accuracy which was previously obtained only with bubble chambers. The main aim of the experiment was to search for the oscillation  $\nu_\mu$  into  $\nu_\tau$ , in a region of mass compatible with the prescriptions of the hot dark matter hypothesis, which predicted a  $\nu_\tau$  mass in the range of 1–10 eV/c<sup>2</sup>. This was done by searching for  $\nu_\tau$  CC interactions, observing the production of the  $\tau$  lepton through its various decay modes by using kinematical criteria. In parallel, NOMAD also strongly contributed to the study of more conventional processes: quasielastic events, strangeness production and charm dimuon production, single photon production, and coherent neutral pion production. Exotic searches were also investigated. The paper reviews the neutrino beam, the detector setup, the detector performances, the neutrino oscillation results, the strangeness production, the dimuon charm production, and summarizes other pieces of research.

## 1. Motivation

When it was proposed, the experiment was motivated by theoretical arguments suggesting that the  $\nu_\tau$  may have a mass of 1 eV/c<sup>2</sup> or higher, and therefore could be the main constituent of the dark matter in the Universe. This suggestion was based on two assumptions:

- (i) the interpretation of the solar deficit in terms of  $\nu_e \rightarrow \nu_\mu$  oscillations, amplified by matter effects inside the Sun, giving  $\Delta m^2 \sim 10^{-5} \text{ eV}^2/c^4$ ;
- (ii) the so-called “see-saw” mechanism which predicted that neutrino masses are proportional to the square of the mass of the charged lepton or the charge 2/3 quark of the same family.

Furthermore, in analogy with quark mixing, neutrino mixing angles were expected to be small. This defined the region to search for the corresponding oscillation.

To fulfill this program, the NOMAD detector measured and identified most of the particles, charged and neutral, produced in neutrino interactions. The active target was a set of drift chambers with a fiducial mass of about 2.7 tons

and a low average density (99 kg/m<sup>3</sup>) comparable to liquid hydrogen. The detector was located in a dipole magnet, formerly used by the UA1 experiment, giving a field of 0.4 T. This allowed a determination of the momenta of charged particles via their curvature, with minimal degradation due to multiple scattering. The active target was followed by a transition radiation detector to identify electrons, an electromagnetic calorimeter including a preshower, a hadronic calorimeter, and, finally, a muon system.

The  $\tau$  was searched for via its CC interactions:  $\nu_\tau + N \rightarrow \tau + X$ . Given the lifetime of the  $\tau^-$  and the energies considered here, the  $\tau^-$  travelled about 1 mm before decaying. The spatial resolution of NOMAD, while good, was not sufficient to recognize the nonzero impact parameter associated with such tracks. Instead, the decay of the  $\tau^-$  was identified using kinematical criteria, based on a precise measurement of the missing transverse momentum in the final state. This required a detector with accurate energy and momentum resolution, good particle identification, and sophisticated analysis schemes.

In order to be sensitive to a large fraction of the  $\tau^-$  decay modes and to be able to select events with high acceptance

and low backgrounds, the NOMAD detector had to fulfill the following criteria:

- (i) measurement of the momenta of charged particles with good precision and
- (ii) identification and measurement of electrons, photons, and muons.

The excellent performances of the NOMAD detector fulfilled these goals.

In addition to searching for neutrino oscillations, the large sample of well-reconstructed data collected with a target having the density of a hydrogen bubble chamber, permitted to study many other processes involving neutrinos.

The Monte Carlo (MC) simulation used throughout this study was based on modified versions of LEPTO 6.1 and JETSET 7.4 generators for neutrino interactions and on a GEANT-based program for the detector response.

## 2. The Beam

The NOMAD detector was located at the CERN west area neutrino facility (WANF) and was exposed to the SPS wide-band neutrino beam consisting predominantly of  $\nu_\mu$ 's. The beam line has been operating for 20 years and was reoptimized in 1992-1993 for the NOMAD and CHORUS experiments. Details of operations are given in [1].

The neutrinos were predominantly produced from the decays in flight of the secondary  $\pi$  and  $K$  mesons originating from the 450 GeV protons impinging on a beryllium target. The SPS cycle was repeated every 14.4 s. The protons were extracted from the SPS in two 4 ms long spills separated by 2.6 s with a 2.0 s "flat top." The beam line operated with record intensities up to  $1.8 \cdot 10^{13}$  protons in each of the two spills. During the four years of data taking, 1995-1998, NOMAD collected a total of  $2.2 \cdot 10^{19}$  protons incident on the target.

The target station consisted of 11 beryllium rods separated by 9 cm gaps. Each rod was 10 cm long and 3 mm in diameter, positioned longitudinally along the proton line. The secondary pions and kaons were focused by a pair of coaxial magnetic lenses, called the horn and the reflector. In such a system, charged particles were deflected by the toroidal field between two coaxial conductors carrying equal and opposite currents so that the focusing of particles of one sign implied defocusing particles of the opposite sign. In order to harden the neutrino spectrum, the horn and reflector were displaced 20 m and 90 m from the target, respectively. The higher neutrino energy increased the sensitivity of the experiment to charged current  $\nu_\tau$  interactions which have an energy threshold of 3.5 GeV. The sections between the horn and the reflector and between the reflector and the decay tunnel were enclosed in helium tubes of 80 cm diameter and a total length of about 60 m in order to reduce the absorption of secondary particles. Collimators reduced the antineutrinos contamination by intercepting the defocused secondaries.

The mesons were allowed to decay in a 290 m long vacuum tunnel. Shielding made from iron and earth followed. Its use was to range out muons and absorb hadrons. A toroidal magnet, operated at 3 kA located at the entrance of the iron

shielding, deflected muons which would pass outside the shielding. The NOMAD detector was located 835 m from the target. The average distance between the meson decay points and NOMAD was 620 m.

A neutrino beam monitoring system based on the detection of muon yields at several depths into the iron shield was built. Silicon detectors provided an absolute flux measurement. An independent measurement of the flux was given by the number of protons incident on the target, estimated from a pair of beam current transformers (BCT) upstream of the target.

A detailed GEANT simulation of the beam line predicted the neutrino energy and radial position distributions. Figure 1 shows the neutrino flux for  $10^9$  protons on target. The Monte Carlo simulation predicted the relative abundance of neutrino species:  $\nu_\mu : \text{anti}\nu_\mu : \nu_e : \text{anti}\nu_e = 1.00 : 0.061 : 0.0094 : 0.0024$  with average energies of 23.5, 19.2, 37.1, and 31.3 GeV, respectively.

Since the search consisted in observing  $\nu_\tau$  interactions, it was essential to calculate the intrinsic  $\nu_\tau$  component in the beam. This component came from the prompt reactions:

$$p + N \longrightarrow D_s + X, \quad (1)$$

$$\text{followed by } D_s \longrightarrow \tau + \nu_\tau, \quad \tau \longrightarrow \nu_\tau + X.$$

The relative number of  $\nu_\tau$  produced from the above reactions and interacting via the CC channel in the fiducial volume of NOMAD was estimated to be  $5 \cdot 10^{-6}$  with respect to  $\nu_\mu$  CC interactions. The resulting intrinsic  $\nu_\tau$  signal was much less than one event in the total duration of the NOMAD experiment.

## 3. The Detector

The detector is shown schematically in Figure 2. It consisted of a number of subdetectors most of which were located in a large dipole magnet, having an inner volume of 7.5 m along the beam axis and  $3.5 \times 3.5 \text{ m}^2$  in transverse dimensions. The coordinate system adopted for NOMAD had the  $x$ -axis into the plane of the figure, the  $y$ -axis directed up towards the top of the detector and the  $z$ -axis horizontal, approximately along the direction of the neutrino beam. The beam line pointed upwards, at an angle of  $2.4^\circ$  with the  $z$ -axis. The magnetic field was along the  $x$ -axis and had a value of 0.4 T.

Moving downstream along the beam direction came a veto counter, a front calorimeter, a large active target consisting of drift chambers, a transition radiation detector, a preshower, an electromagnetic calorimeter, a hadron calorimeter, and an iron filter consisting in the return-yoke of the magnet followed by a set of large drift chambers used for muon identification. Upstream and downstream of the transition radiation detector, two large hodoscopes of scintillators provided a fast trigger. The key features of each subdetector are given below. Overall, the detector reconstructed the events kinematics with great precision and identified electrons, muons, and photons.

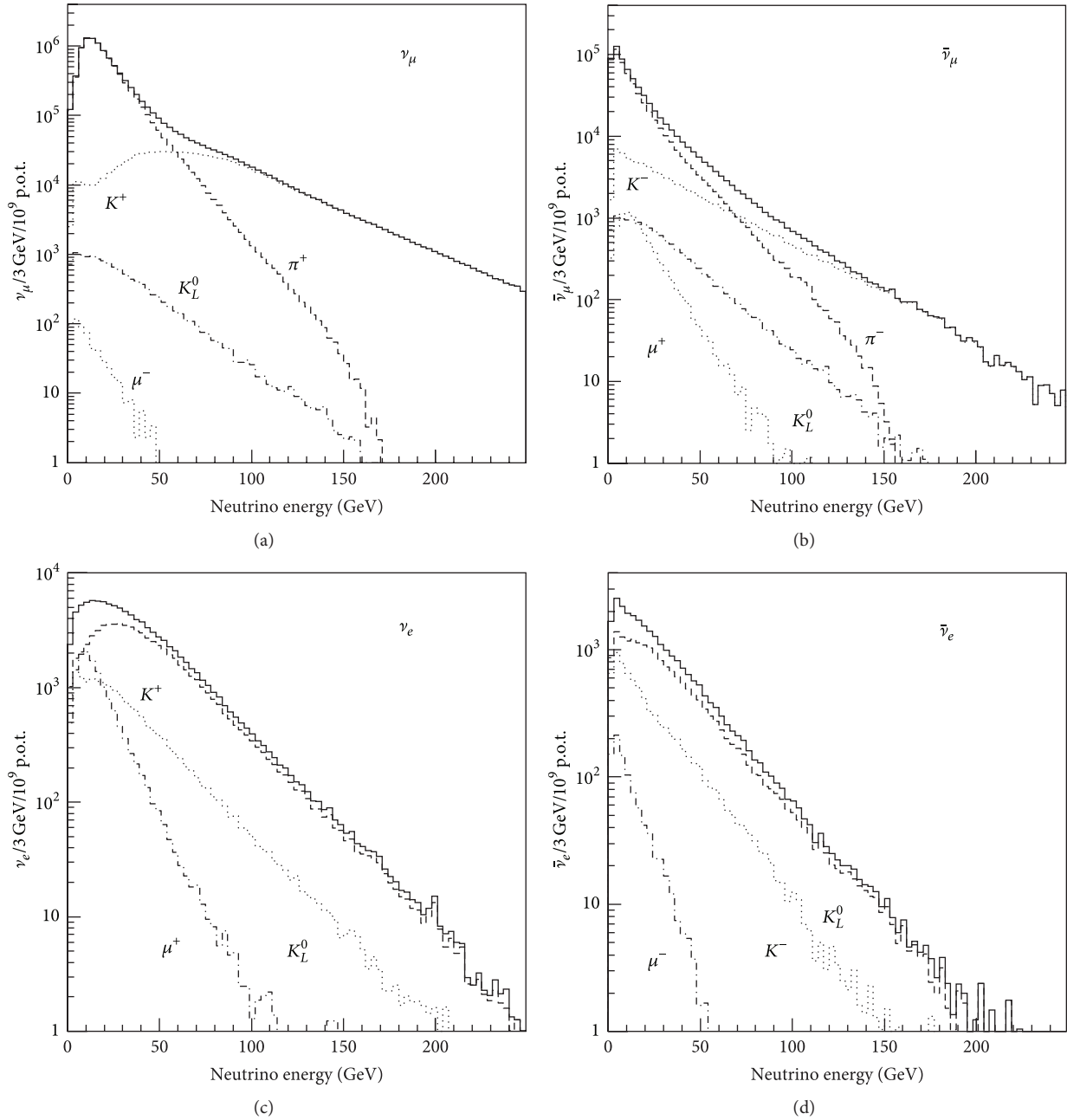


FIGURE 1: Fluxes of the various neutrino species in the NOMAD detector for  $10^9$  protons on target (from [1]).

**3.1. Veto Counters.** The veto system consisted of an arrangement of 59 scintillation counters covering an area of  $5 \times 5 \text{ m}^2$  at the upstream end of the detector. The counters were arranged in a geometry which provided optimal rejection of charged particles produced in neutrino interactions upstream of NOMAD, for example, in the iron magnet support, and large-angle cosmic rays travelling in the same or the opposite direction to the neutrino beam.

The two photomultiplier outputs connected to each scintillator counter were fed to the inputs of mean-timer modules, the timing of which provided an output signal independent in time of the position at which the detected

charged particle traversed the counter. The charged particle rejection efficiency of the NOMAD veto was constantly monitored and remained stable at a level of 96-97%. Averaged over the two neutrino spills, the contribution of the veto system to the overall dead time of NOMAD was 4%.

**3.2. The Front Calorimeter (FCAL).** The detector was suspended from iron pillars at the two ends of the magnet. The front pillar was instrumented with scintillator planes to provide an additional massive active target for neutrino interactions. The FCAL consisted of 23 iron plates and 4.9 cm thick and separated by 1.8 cm gaps. Twenty out of the 22 gaps

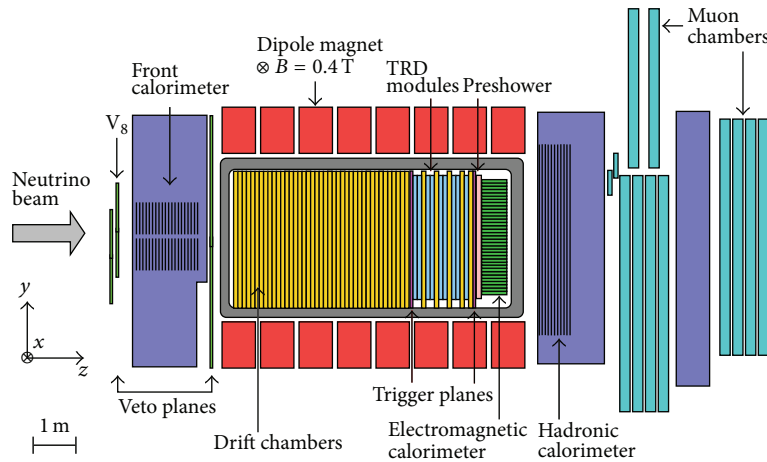


FIGURE 2: A schematic sideview of the detector.

were instrumented with long scintillators read out on both ends. The dimensions of the scintillators were  $175 \times 18.5 \times 0.6 \text{ cm}^3$ .

The FCAL had a depth of about 5 nuclear interaction lengths and a total mass of about 17.7 tons. A minimum ionizing particle traversing the whole FCAL had an equivalent hadronic energy of 430 MeV. The FCAL was particularly useful for the study of charm dimuon production.

**3.3. The Drift Chambers (DC).** The drift chambers [2] were a crucial part of the detector. They provided the target material and the tracking device for the particles. They were designed with the conflicting requirements that their walls should be as heavy as possible in order to maximize the number of neutrino interactions and as light as possible in order to minimize multiple scattering of particles, secondary particle interactions, and photon conversions. To minimize the total number of radiation lengths ( $X_0$ ) for a given target mass, the chambers were made of low density and low atomic number materials. The complete target consisted of 145 drift chambers, with a total mass of 2.9 tons over a fiducial area of  $2.6 \times 2.6 \text{ m}^2$ . Each chamber contributed  $0.02X_0$ . Overall, the target had a density of  $0.1 \text{ g/cm}^3$  and a total length of  $1.0X_0$ ; there was less than  $0.01X_0$  between two consecutive hit measurements in the chamber planes.

The chambers were built on panels made of aramid fibres in a honeycomb structure. These panels were sandwiched between two Kevlar-epoxy resin skins. These skins gave the mechanical rigidity and flatness necessary over the large  $3 \times 3 \text{ m}^2$  surface area. Each drift chamber consisted of four panels. The three 8 mm gaps between the panels were filled with an argon-ethane (40%–60%) mixture at atmospheric pressure. The gas was circulating permanently in a closed circuit with a purifier section that removed oxygen and water vapor.

The central gap was equipped with sense wires at  $+5^\circ$  and  $-5^\circ$  with respect to the magnetic field direction. These sense wires were  $20 \mu\text{m}$  in diameter and were made of gold-plated tungsten. They were interleaved with  $100 \mu\text{m}$  potential wires made of Cu-Be. These wires were equally spaced vertically to

provide drift cells of  $\pm 3.2 \text{ cm}$  around each sense wire. Field shaping aluminum strips were printed on mylar glued to the panels. The 3 m long wires were glued to support rods at three points to keep them at a constant 4 mm distance from the cathode planes. The gap was maintained at 8 mm using nine spacers facing melanine inserts embedded in the honeycomb structure of the panels. The potential wires were held at  $-3200 \text{ V}$  and the anode wires at  $+1750 \text{ V}$ . The potentials on the strips provided a drift field of  $1 \text{ kV/cm}$ . With this electric field and the gas mixture used, the ionization electrons drifted with a velocity of about  $50 \text{ mm}/\mu\text{s}$ . In order to compensate for the Lorentz angle and to keep a drift direction parallel to the planes when the magnetic field was turned on, the potentials on the strips were set at different values on the two sides of each gap.

There were 49 chambers in the complete detector, each corresponding to 147 sense wire planes for a total of 6174 wires. The target chambers were mounted in 11 modules of four chambers in the front part of the detector and five additional chambers were installed individually in the TRD region and were used to improve the lever arm for tracking and for better extrapolation of the tracks to the rest of the subdetectors.

The typical wire efficiency was 97%, most of the loss being due to the supporting rods. Wire signals were fed to a preamplifier and a fast discriminator, allowing track separation down to 1 mm. The spatial resolution was studied using straight tracks (muons) crossing the detector during data taking. The distribution of residuals was obtained after a careful alignment of all wires as well as a detailed description of the time-to-distance relation. The distribution had a sigma of about  $150 \mu\text{m}$ . The  $5^\circ$  stereo angles gave a resolution along the wires of 1.5 mm.

The momentum resolution provided by the drift chambers was a function of momentum and track length. For charged hadrons and muons travelling normal to the plane of the chambers, it was parameterized as

$$\frac{\sigma_p}{p} \sim \frac{0.05}{\sqrt{L}} + \frac{0.008p}{\sqrt{L^5}}, \quad (2)$$

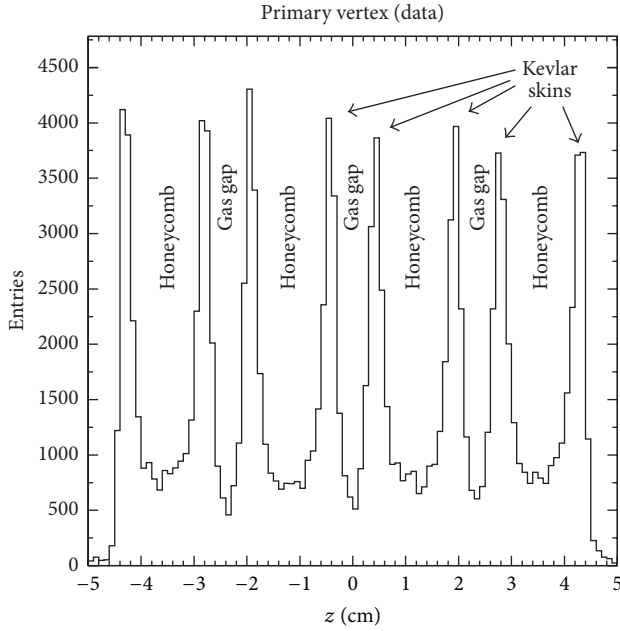


FIGURE 3: Distribution of vertices through one drift chamber along the beam direction (from [3]).

where the momentum  $p$  is in GeV/c and the track length  $L$  in m. The first term is the contribution from multiple scattering and the second term comes from the single hit resolution of the chambers. For a momentum of 10 GeV/c, multiple scattering was the dominant contribution for track lengths larger than 1.3 m.

The tracking was more difficult for electrons as they radiated photons via bremsstrahlung process as they traversed the nonzero-density tracking system. This resulted in a continuously changing curvature. In this case the resolution was worse and electron energies were measured by combining information from the drift chambers and the electromagnetic calorimeter.

Most neutrino interactions in the NOMAD active target occurred in the passive panels of the drift chambers. Interaction vertices were reconstructed by extrapolating the tracks of charged secondary interaction products. Figure 3 shows the distribution of vertices along the beam direction showing the structure of a set of DC's. The eight "spikes" in this distribution correspond to the Kevlar skins of the DC's. Regions with a low interaction rate correspond to the three gas-filled drift gaps of the honeycomb panels. This figure directly shows the vertex reconstruction resolution.

**3.4. The Trigger Counters.** Two trigger planes were installed in the NOMAD detector. The first followed the active target and the second was positioned behind the TRD region. Each of the planes covered a fiducial area of  $280 \times 286 \text{ cm}^2$  and consisted of 32 scintillation counters. The scintillators had a thickness of 0.5 cm and a width of 19.9 cm. Twenty-eight of the counters were installed horizontally and had a length of 124 cm. In order to increase the fiducial area of the trigger planes, four counters of 130 cm length were installed vertically to cover the light-guides of the horizontal counters.

The scintillators were connected by adiabatic light-guides to 16-dynode photomultipliers which were oriented parallel to the magnetic field. The field of 0.4 T only reduced the response of the tubes by 30%. They had an intrinsic time resolution of 1 ns and a noise rate of less than 50 Hz. A coincidence between the two planes was required for a valid trigger. The average efficiency of the trigger counters, for single tracks, was determined with data and found to be  $(97.5 \pm 0.1)\%$ .

**3.5. The Transition Radiation Detector (TRD).** The NOMAD TRD [4, 5] was designed to separate electrons from pions with a pion rejection factor greater than  $10^3$  for a 90% electron efficiency in the momentum range from 1 to 50 GeV/c. This factor, together with the additional rejection provided by the preshower and the electromagnetic calorimeter, was specially needed in the search for the electronic  $\tau$  decay channel in order to eliminate neutral current (NC) interactions in which an isolated pion track could fake an electron.

The large rejection factor required and the large lateral dimensions of the detector ( $2.85 \times 2.85 \text{ m}^2$ ) made the NOMAD TRD one of the largest transition radiation detectors ever built. Its design was optimized by detailed simulation and after several test beam measurements. It took into account two main experimental constraints: the limited longitudinal space inside the NOMAD magnet and the requirement that there be less than  $2\%X_0$  added between two consecutive hit measurements in the drift planes.

The TRD was located after the first trigger plane and consisted of nine identical modules. The first eight modules were paired into four doublets. In order to provide a precise track extrapolation from the drift chamber target to the calorimeter, five drift chambers were embedded in the TRD, one after each TRD doublet and one after the last module.

Each TRD module included a radiator followed by a detection plane with the following design.

- (i) The radiator was a set of 315 polypropylene foils, each  $15 \mu\text{m}$  thick and  $2.85 \times 2.85 \text{ m}^2$  in area, separated by  $250 \mu\text{m}$  air gaps. The foils were stretched on an aluminum frame and embossed to ensure a regular spacing in spite of their large size and electrostatic effects.
- (ii) The detection plane consisted of 176 vertical straw tubes, each 3 m long and 16 mm in diameter, separated by 0.2 mm. The straw tubes were fed in parallel with a xenon-methane (80%–20%) gas mixture. They were made of two shifted  $12.5 \mu\text{m}$  thick ribbons of aluminized mylar rolled and glued along a 16 mm diameter helix. The sensitive anode was a  $50 \mu\text{m}$  diameter gold-plated tungsten wire stretched with a tension of 100 g.

The signals from the 1584 straw tubes were fed into amplifiers producing differential outputs. The charge ADCs were read out by a VME system. A test pulse system was used to control the stability of the entire electronic chain. Continuous calibration of the TRD was performed with the help of  $^{55}\text{Fe}$  radioactive sources uniformly deposited

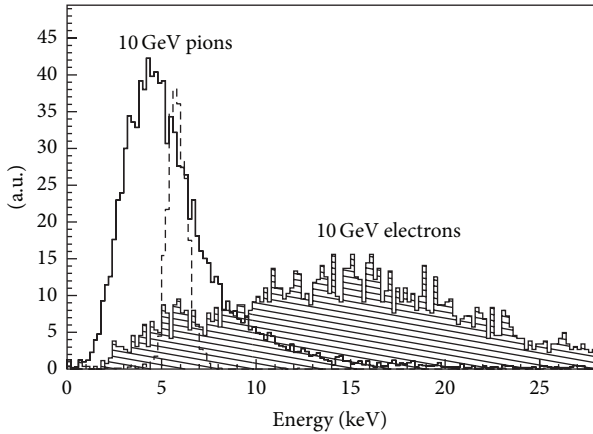


FIGURE 4: Energy deposited in the TRD straw tubes for pions and electrons (from [4, 5]).

on a ribbon stretched horizontally in the middle of each detection plane.

Electron identification in the TRD was based on the difference in the total energies deposited in the straw tubes by particles of different Lorentz factors ( $\gamma = E/mc^2$ ). Charged particles with  $\gamma < 500$  deposited energy predominantly by ionization losses, whereas charged particles with  $\gamma > 500$  (mainly electrons) also produced transition radiation X-rays at the interfaces of the foils. As a result, a few photons in the keV range were produced by an electron crossing a radiator. About 60% of the photons emitted from the radiator were absorbed in the detection planes due to the large cross-section of xenon for photons of a few keV. Transition radiation X-ray energy deposition was added to the ionization losses of the parent particle in the same straw tube, because the emitted photons peaked around the initial particle direction.

The algorithm developed for electron identification was based on a likelihood ratio method. Figure 4 shows the normalized spectra (MC simulation) of energy deposited in the TRD straw tubes by 10 GeV/c pions and electrons at normal incidence. The TRD simulation was extensively tested *in situ* using muons crossing the detector during the flat top between two neutrino spills.

A pion rejection factor greater than 1000 was obtained with the 9 TRD modules in the momentum range from 1 to 50 GeV/c, while retaining an electron efficiency of 90%.

**3.6. The Preshower Detector (PRS).** The PRS was located just in front of the electromagnetic calorimeter. It was composed of two planes of proportional tubes (286 horizontal and 288 vertical) preceded by a 9 mm ( $1.6X_0$ ) lead-antimony converter.

The proportional tubes were made of extruded aluminum profiles and glued to two aluminum end plates of 0.5 mm thickness. Each tube had a square cross-section of  $9 \times 9 \text{ mm}^2$  and the walls were 1 mm thick. The  $30 \mu\text{m}$  gold-plated tungsten anode was strung with a tension of 50 g. The proportional tubes operated at a voltage of 1500 V, with a mixture of Ar-CO<sub>2</sub> (80%–20%). Signals from each tube were

fed into charge preamplifiers; the twelve preamplifier signals were sent to ADCs.

Large samples of straight through muons were collected during the flat top of the SPS cycle. The fine granularity of the PRS assisted in the understanding of signals in the calorimeter blocks caused by adjacent particles. Once the clusters with an associated track had been removed, the remaining ones could be attributed to photons which converted in the PRS. The resolution was estimated using negative pions from a test beam interacting in the lead of the PRS. It was assumed that these interactions came mainly from charge exchange with one of the photons from a  $\pi^0$  converting in the lead plate. The r.m.s. resolution for these events was 1 cm, a value much smaller than the dimensions of a single tower of the electromagnetic calorimeter which allowed the use of the PRS to determine the impact point of converting photons for the 70% of the photons which converted in the lead radiator. Using the above value as the spatial resolution of photons and the energy resolution of the electromagnetic calorimeter, a rough estimation of the  $\pi^0$  mass resolution was found to be  $11 \text{ MeV}/c^2$ , which is in good agreement with the observed  $\pi^0$  mass distribution.

**3.7. The Electromagnetic Calorimeter (ECAL).** The search for  $\nu_\tau$  events in NOMAD relied strongly on electron identification as well as on a very accurate determination of the transverse momentum in the event. While electron identification was performed using the TRD, the ECAL was crucial to accurately measure electron and gamma energies from 100 MeV up to 100 GeV and to help in the determination of the neutral component of the transverse momentum. The large energy range to be covered required a large dynamic range in the response of the detector and of the associated electronics. A lead-glass detector was chosen for its excellent energy resolution and uniformity of response. The ECAL [6, 7] combined with the PRS was also used to help improve the electron identification provided by the TRD.

The ECAL consisted of 875 lead-glass Cherenkov counters of the TF1-000 type arranged in a matrix of 35 rows and 25 columns. Each counter was a  $19X_0$  deep block with a rectangular cross-section of  $79 \times 112 \text{ mm}^2$ . The direction of the magnetic field, perpendicular to the counter axis, imposed severe constraints on the mechanical assembly of the light detection system. The light detectors (two-stage photomultiplier tetrodes, with a typical gain of 40 in the operating conditions) were coupled to the back face of the lead-glass blocks. This face was cut at  $45^\circ$  with respect to the block axis, in such a way that the symmetry axis of the tetrodes formed an angle of  $45^\circ$  with respect to the field direction, thus keeping the signal reduction caused by the magnetic field less than 20%. This reduction was found to be very constant and uniform. A low-noise electronic chain composed of a charge preamplifier followed by a shaper and a peak sensing ADC provided a calorimeter response in a dynamic range larger than 4000.

A fast analog signal from each shaper was also provided for time measurements in order to reject energy depositions not associated with triggered events. The obtained time

resolution was a few ns for energy depositions larger than 1 GeV. In addition, the fast analog signals, summed over groups of 64 counters, formed an ECAL trigger.

Monitoring of the lead-glass response was performed using two blue LED's per counter mounted on the same face of the block on which the tetrodes were positioned. Before the final assembly in NOMAD, the lead-glass blocks were individually calibrated using a 10 GeV/c electron beam. The effect of the field on the calibration was taken into account by LED measurements performed with and without magnetic field.

The linearity of the calorimeter response to electrons was verified at the test beam in the energy range 1.5–80 GeV. A detailed study of the energy resolution was performed. A two-parameter fit of the energy resolution  $\Delta E/E = a+b/\sqrt{E}$ , with  $E$  in GeV, gave  $a = (1.04 \pm 0.01)\%$  and  $b = (3.22 \pm 0.07)\%$ .

The ECAL response as a function of the impact point of the incoming electrons was measured to be uniform within  $\pm 0.5\%$ ; the response to electrons entering at normal incidence in the gaps between adjacent blocks showed that ECAL was “hermetic” at more than 99%. A weak dependence of the total energy release on the angle of incidence  $\theta$  of the incoming electrons was found both in the test beam measurements and in the MC simulations. This dependence could be attributed to the small variation with the angle of the Cherenkov light collection efficiency. In addition, the number of towers receiving contributions from a given shower increased with angle. However this did not affect the overall energy resolution that remained insensitive to both shower position and angle. The shower position was measured with an average resolution of about 4 mm in each direction.

The calibration and the calorimeter response to low energy photons were checked by measuring the  $\pi^0$  mass both in a dedicated test beam and during the NOMAD data taking. The following results were found using test beam data:

$$m_\pi = (133.7 \pm 1.2) \text{ MeV}/c^2 \quad \text{with } \sigma_m = 16 \text{ MeV}/c^2. \quad (3)$$

The calorimeter response to muons corresponded to a peak value for the energy deposition of  $(0.566 \pm 0.003) \text{ GeV}$ . The muon signals were found to be stable within  $\pm 1\%$  providing an independent check of the stability in the calorimeter response.

**3.8. The Hadronic Calorimeter (HCAL).** The HCAL was intended to detect neutral hadrons and to provide a measurement of the energy of charged hadrons complementary to that derived from momentum measurements in the DC's. Knowledge of neutral hadrons was important when attributing kinematic quantities such as missing transverse momentum. Furthermore calorimetric measurements of charged particles were used both as a consistency check on the momentum measurements of the charged particles and as an aid in distinguishing between muons and charged hadrons.

The HCAL was an iron-scintillator sampling calorimeter. The downstream iron pillar of the magnet was instrumented with scintillators. It consisted of 23 iron plates, 4.9 cm thick

separated by 1.8 cm gaps, six of these modules forming a wall of 5.4 m wide, 5.8 m high, and 1.5 m deep. This wall acted as a filter for the system of large muon chambers set up downstream.

The active elements of the calorimeter were scintillator paddles 3.6 m long, 1 cm thick, and 18.3 cm wide. Tapered acrylic light pipes were glued to each end of the scintillator paddles to form an assembly 5.52 m long. Eleven of these assemblies were threaded horizontally through the first 11 gaps in the iron wall to form a calorimeter module 18.3 cm high and approximately 3.1 interaction lengths deep. Scintillation light was directed through adiabatic light guides to a 5 inch phototube at each end of the module. Eighteen of these modules were stacked vertically to form a calorimeter with an active area 3.6 m wide by 3.5 m high.

The energy deposited in a given module was obtained from the geometric mean of the two phototube signals, and the horizontal position of the energy deposit was determined from the attenuation length of the scintillator and the ratio of the phototube signals. Vertical positions were determined from the pattern of energy sharing between the modules. The energy response to muons which traversed the calorimeter gave a peak corresponding to the minimum ionizing distribution at 1.5 GeV with the expected Landau shape.

Typical position resolutions were of the order of 20 cm in the horizontal projection. There was a high probability for hadrons to begin showering upstream of the hadron calorimeter and so the total hadronic energy was taken to be a weighted sum of the energies deposited in the hadron and electromagnetic calorimeters.

**3.9. The Muon Chambers.** The NOMAD muon detector consisted of 10 drift chambers previously used in the UA1 experiment. Each chamber had an active area of  $3.75 \times 5.55 \text{ m}^2$  with two planes of drift tubes in the horizontal and two in the vertical directions. In total there were 1210 drift tubes, each with a maximum drift distance of 7 cm.

The chambers were arranged in pairs (modules) for track segment reconstruction. The first muon station consisted of three modules and was placed behind the hadron calorimeter. It was followed by an 80 cm thick iron absorber and a second muon station of two modules.

The chambers were operated with an argon-ethane (40%–60%) gas mixture. Their performance was monitored continuously using high energy muons passing through the detector. The average position resolution for hits was in the range of 350–600  $\mu\text{m}$  depending on the gas quality. The average hit efficiency was 92.5% and the dominant source of inefficiency (6.5%) was due to dead areas between the drift tubes.

Track segments were reconstructed separately for each station from typically 3 or 4 hits per projection. The measured efficiency for the reconstruction of track segments was 97%.

**3.10. Triggering and Data Acquisition System.** The trigger logic [8] was performed by a VME-based module, which was especially designed for NOMAD. The following triggers were set up for the study of neutrino interactions in NOMAD.

- (i)  $\underline{V}.T_1.T_2$ . This trigger allowed a study of neutrino interactions in the DC target region. At least one hit in both trigger planes  $T_1$  and  $T_2$  was required. To prevent triggering on through-going muons, no hit should have occurred in the veto counters ( $\underline{V}$ ). The rate for this trigger was  $\sim 5.0/10^{13}$  p.o.t. and the lifetime was  $(86 \pm 4)\%$ . Of these 5 triggers, about 0.5 were potentially interesting candidates for neutrino interactions in the DC. The remaining triggers consisted of 1 “cosmics,” 1.5 nonvetoed muons, and 2 neutrino interactions in the magnet.
- (ii)  $\underline{V}_8.FCAL$ . Neutrino interactions in the front calorimeter with an energy deposition of at least 4 m.i.p. fired this trigger. Through-going muons were vetoed by the veto subset  $\underline{V}_8$ . On average 6.5 neutrino interactions occurred in the FCAL for  $10^{13}$  p.o.t. The lifetime was  $(90 \pm 3)\%$ .
- (iii)  $\underline{V}_8.T_1.T_2.FCAL$ . This trigger was set up to study quasielastic-like events in the FCAL. For this trigger, an energy deposition between 1 and 3 m.i.p. in the FCAL was requested. The rate for this trigger was  $\sim 1.5/10^{13}$  p.o.t. and the lifetime was  $(90 \pm 3)\%$ .
- (iv)  $T_1.T_2.ECAL$ . The electromagnetic calorimeter was also used as a target. Physics topics addressed with these events included  $\nu_\mu \rightarrow \nu_e$  and  $\nu_\mu \rightarrow \nu_\tau$  oscillations. An energy deposition of more than  $\sim 1.0$  GeV in the ECAL enabled this trigger, which had an average rate of  $2/10^{13}$  p.o.t. and a lifetime of  $(88 \pm 3)\%$ .
- (v) RANDOM. A random trigger allowed a study of detector occupancy.

Approximately 15 neutrino candidate triggers were taken in each neutrino spill. In addition various triggers were used in the 2.6 s long flat-top between the two neutrino bursts. These were used for drift chamber alignment, calibration of the different subdetectors, and measurement of the trigger counter efficiency. In total about 60 triggers were taken in each flat top. NOMAD operated in burst mode, where triggers arrive in short intervals (spills) separated by relatively long intervals without beam. Signals from each subdetector arrived at some combination of the three types of FAST-BUS modules: 12-bit charge-integrating ADCs, 12-bit peak-sensing ADCs, and 16-bit TDC's. There were a maximum of 11648 channels to read out per event.

Five VME-based boards controlled the readout of the front-end electronics. The VME controllers performed block transfers of the available data to local buffers, assembled the data into subevents, and checked for consistency and integrity. They then passed the subevents through a VME interconnect bus to a sixth VME processor, the “event builder,” which assembled all the pieces into complete events together with information about the beam extraction and wrote them to one of two 9 GB disks via a high-level networking package. The event-builder stage also asynchronously received beam calibration data, summaries of monitoring information, and detector status information whenever they changed.

Monitoring programs for each of the nine subdetectors as well as for beam, scaler, and trigger information connected to the stages via Ethernet and generated summary histograms to verify the quality of the data. The system recorded over 1.5 MB of data per minute, with a typical assembled neutrino event containing around 2000 32-bit words before reconstruction. During neutrino spills, the data acquisition had a typical dead time of 10% arising from digitizations. The data-taking time lost due to downtime and interrun transitions was less than 3%.

## 4. Detection Performances

Figure 5 shows a candidate  $\nu_\mu$  CC event detected in NOMAD. One energetic particle penetrates to the muon chambers and satisfies all other criteria to be a muon. A hadronic jet of charged particles is clearly visible at the primary vertex and a photon conversion in the drift chambers is also evident.

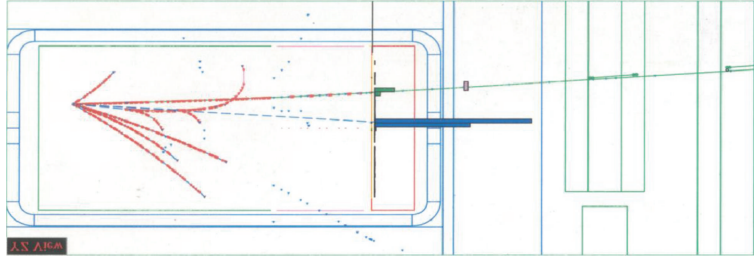
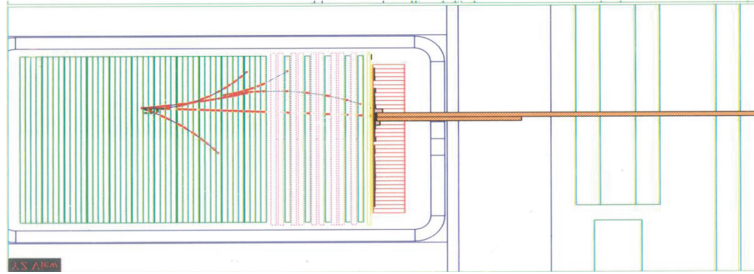
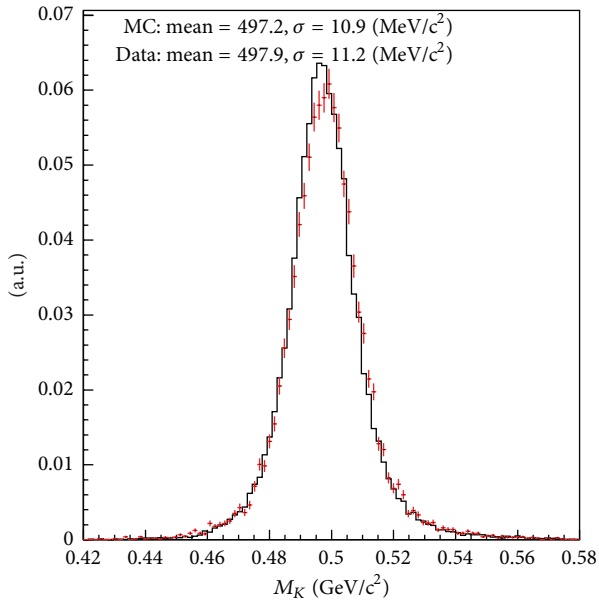
Figure 6 shows a candidate  $\nu_e$  CC event detected in NOMAD. One very straight secondary track identified as an electron by the TRD is seen to deposit a large amount of energy in a few cells of the ECAL as indicated by the large “bar” in the event display.

4.1. *Identification of  $K^0$ .  $K_s^0$  mesons observed in NOMAD were used as a quality check of the reconstruction program and of the detector performance. Using an algorithm looking for  $V^0$  vertices, Figure 7 shows the  $\pi^+\pi^-$  mass distribution obtained from the neutrino beam data, where the following selection criteria were applied:*

- (i) a pair of oppositely charged tracks, not positively identified as electrons or muons, emerging from a secondary vertex distinct from the primary;
- (ii) the reconstructed momentum of the pair pointing to the primary vertex;
- (iii) the invariant mass of the pair differing from the  $\Lambda^0$  mass by more than  $50 \text{ MeV}/c^2$ , when taken to be a combination  $p\pi^-$ .

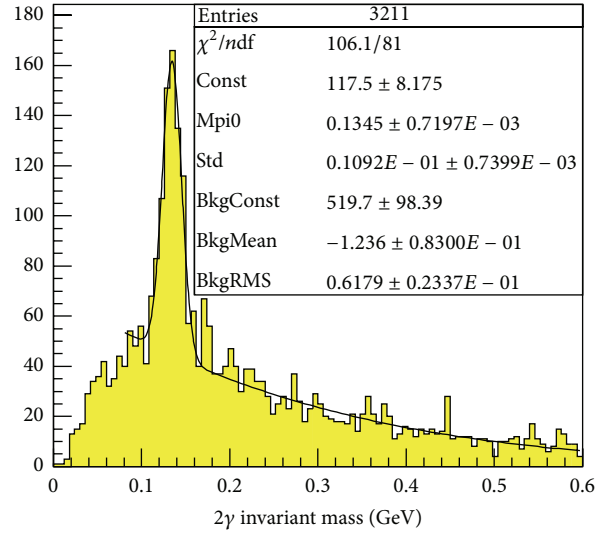
The  $K^0$  peak stood out clearly over a small background. A fit gave a value for the mass of  $(497.3 \pm 0.4) \text{ MeV}/c^2$ . The resolution was  $11 \text{ MeV}/c^2$ , consistent with the measured momentum resolution of NOMAD. The proper distance travelled by the  $K_s^0$  before decaying gave a lifetime of  $(892 \pm 65)10^{-13}$  s in agreement with the known value.

4.2. *Reconstruction of  $\pi^0$  Mesons.* Gamma rays from  $\pi^0$  decays represented the best electromagnetic probe available in NOMAD to test the ECAL response. The  $\pi^0$  flux was too small to allow individual calibration of each ECAL block, but allowed a test of the overall energy response. Figure 8 shows the  $2\gamma$  invariant mass distribution obtained from the data for two-charged-tracks events with a vertex in the DC region and two neutral clusters in the ECAL. The peak position is well centered on the  $\pi^0$  mass and the width ( $11 \text{ MeV}/c^2$ ) is in good agreement with the expected resolution.

FIGURE 5: Candidate  $\nu_\mu$  CC event reconstructed in the NOMAD detector.FIGURE 6: Candidate  $\nu_e$  CC event reconstructed in the NOMAD detector.FIGURE 7:  $\pi^+\pi^-$  mass distribution showing the signal of  $K^0$  (from [9]).

**4.3. Muon Identification.** Muons were identified if they penetrated more than 8 interaction lengths of absorber material in order to reach the first station or 13 interaction lengths for the second station of the muon system. For perpendicular incidence, the momentum to reach the chambers was measured to be 2.3 GeV/c for station 1 and 3.7 GeV/c for station 2. The geometrical acceptance to hit either of the two stations was about 98%. This number applied to primary muons from  $\nu_\mu$  CC interactions averaged over their production point.

The muon momentum was measured in the central drift chambers with a precision of 3% for momenta below

FIGURE 8:  $2\gamma$  invariant mass distribution showing the signal of  $\pi^0$  (from [3]).

20 GeV/c, where the error was dominated by multiple scattering. For larger momenta the error slowly rose as measurement errors started to dominate, but the muon charge could be reliably measured for momenta up to 200 GeV/c. The muon reconstruction efficiency was essentially momentum independent above 5 GeV/c and reached more than 95%.

It was very important for many NOMAD analyses to identify events which did not contain a muon. Very low momentum muons could only be eliminated using kinematical criteria, such as  $p_T$  cuts. For muons well above the threshold, the efficiency to detect at least 2 out of 8–16 possible hits was essentially 100% inside the muon chamber geometrical acceptance.

**4.4. Electron Identification.** The NOMAD TRD was designed to separate electrons from heavier charged particles, mainly pions. A “hit” in the TRD was a straw tube with an energy above the pedestal value. A set of hits collected along the road around a drift chamber track was associated with this track. Energy depositions were then compared to the expectations for two possible hypotheses, either electron or pion.

Depending upon the topology of the event, two different identification procedures were applied. The signature of an isolated particle was defined from a likelihood ratio computed from the responses of all the straw tubes crossed by the incident track. The momentum of the particle measured in the DC was taken into account.

The distributions of probability density that a given energy deposition belongs to an  $e$  or  $\pi$  were obtained from detailed simulation, extensive test beam, and *in situ* measurements. A  $\pi$  rejection better than  $10^3$  at 90% electron efficiency was achieved for isolated particles crossing all nine TRD modules in a wide momentum range from 1 to 50 GeV/c.

About 25% of  $\nu_e$  CC interactions lead to tracks having “shared” hits in the TRD. An assignment of a total deposited energy in shared hits to each of the nonisolated tracks would lead to particle misidentification. The identification procedure for nonisolated particles took into account the number of tracks producing each hit and their momenta. For nonisolated tracks one had to consider four hypotheses:  $\pi(p_1)\pi(p_2)$ ,  $e(p_1)\pi(p_2)$ ,  $\pi(p_1)e(p_2)$ , and  $e(p_1)e(p_2)$ , with  $p_1$  and  $p_2$  being the momenta of the tracks. If two tracks had at most three shared hits, the particle identification procedure for isolated tracks was applied to nonshared hits only. If two tracks had more than three shared hits, four likelihood estimators were computed for the energy depositions in shared hits from the corresponding two particle probability distributions. The decision on the nature of the tracks was made by selecting the hypothesis corresponding to the maximum likelihood value.

The procedure allowed a correct identification of 84% of the nonisolated  $\pi$  produced in  $\nu_e$  CC interactions, with 15% of  $\pi\pi$  combinations being misidentified as  $e\pi$  and only 1% as  $ee$ . The performance of the identification algorithms was studied on a sample of muons producing  $\delta$ -ray electrons above 500 MeV/c. With the electron identification algorithm for isolated tracks,  $(86 \pm 3)\%$  of  $\delta$ -ray electrons were correctly identified at a  $10^3$  level of muon rejection.

The electron identification also used the PRS and ECAL in order to substantially improve the  $\pi/e$  separation. In a test beam setup, a rejection factor against pions of about  $10^3$  was obtained in the energy range of 2–10 GeV, while retaining an overall efficiency of 90% to detect electrons.

## 5. Results on the $\nu_\mu \rightarrow \nu_\tau$ Oscillation

The NOMAD experiment was designed to search for  $\nu_\tau$  appearance from neutrino oscillations in the CERN beam. From 1995 to 1998 the experiment collected 1040000 events with an identified muon, corresponding to about 1350000  $\nu_\mu$  CC interactions, given the combined trigger, vertex identification, and muon detection average efficiency of 77%.

The search for  $\nu_\mu \rightarrow \nu_\tau$  oscillations was based on both deep inelastic (DIS) interactions and low-multiplicity (LM) events for all the accessible  $\tau$  decay channels. Details are to be found in [10–13]. The two samples were separated by a cut on the total hadronic momentum  $p_H$  at 1.5 GeV/c. We concentrate on the DIS analysis.

**5.1. Analysis Principle.** From the kinematical point of view,  $\nu_e$  CC events in NOMAD are fully characterized by the (undetected) decay of the primary  $\tau$ . The presence of visible secondary  $\tau$  decay products, here called  $\tau_V$ , allowed to distinguish from NC interactions, whereas the emission of one (two) neutrino(s) in hadronic (leptonic)  $\tau$  decays provided discrimination against  $\nu_\tau$  ( $\nu_e$ ) CC interactions.

The search for  $\nu_e$  CC interactions was performed by identifying most of the  $\tau$  decays:  $\bar{\nu}_e\nu_\tau$ ,  $h^-\bar{\nu}_e\nu_\tau$ ,  $h^-(n\pi^0)\nu_\tau$ , and  $h^-h^+h^-(n\pi^0)\nu_\tau$ , for a total branching ratio of 82.8%.

First, events containing a primary track identified as a muon were rejected. Then neutrino interactions in the active target were selected by requiring the presence of at least one track in addition to the  $\tau$  decay products, having a common vertex in the detector fiducial volume. Quality cuts were applied to ensure that the selected events were properly reconstructed. These requirements, based on approximate charge balance at the primary vertex and on the estimated momentum and energy errors, removed 15% of these events. The candidate particle or system of particles  $\tau_V$  consistent with being produced in  $\tau$  decays was then identified and the associated hadronic system  $H$  was built.

The kinematic selection in each  $\tau$  decay mode was based on a set of global variables which described the general properties of the momenta of the candidate  $\tau_V$  and of the hadronic system  $H$  in the laboratory frame. The variables were selected from the following list.

- (i)  $E_{\text{vis}}$  is the total visible energy of the event.
- (ii)  $\mathbf{p}_V^\tau$  and  $\mathbf{p}^H$  are the total momentum of the visible tau decay product(s) and of the associated hadronic system, respectively.
- (iii)  $E_V^\tau$  is the total energy of the visible tau decay product(s).
- (iv)  $\mathbf{p}_{TV}^\tau$  and  $\mathbf{p}_T^H$  are the components of  $\mathbf{p}_V^\tau$  and  $\mathbf{p}^H$  perpendicular to the neutrino beam direction.
- (v)  $\mathbf{p}_T^m = -(\mathbf{p}_{TV}^\tau + \mathbf{p}_T^H)$  is the missing transverse momentum due to neutrinos from  $\tau$  decay.
- (vi)  $M_T$  is the transverse mass.
- (vii)  $Q_T$  is the component of  $\mathbf{p}_V^\tau$  perpendicular to the total visible momentum vector.
- (viii)  $\theta_{\nu T}$  is the angle between the neutrino direction and the total visible momentum vector.
- (ix)  $\theta_{\nu H}$  is the angle between the neutrino direction and the hadronic jet.
- (x)  $W$  is the invariant effective mass of the hadronic system.

5.2.  $\tau^- \rightarrow e^- \bar{\nu}_e \nu_\tau$ . The search for  $\tau^-$  started with the preliminary identification of the prompt electron in events with no other prompt leptons, followed by kinematical rejection of backgrounds.

The identification of the electron candidate was performed according to strict criteria. Primary electrons were defined as DC tracks with  $p > 1.5 \text{ GeV}/c$  associated with the primary vertex and satisfying requirements based on the TRD identification algorithm, the PRS pulse height, and the ECAL cluster shape. Also a consistency between the associated electromagnetic energy and the measured DC momentum of the candidate was required. Overall, these requirements achieved a charged pion rejection factor of more than  $10^4$ .

Secondary electrons from Dalitz decays and from photons converting close to the primary vertex were suppressed by requiring that the candidate electron did not form an invariant mass of less than  $50 \text{ MeV}/c^2$  with any particle of opposite charge.

These requirements yielded an efficiency of 20% for prompt electrons from  $\tau^-$  decays while accepting only  $2.9 \cdot 10^{-5}$  of  $\nu_\mu$  CC and  $2.0 \cdot 10^{-4}$  of NC interactions.

Then the kinematical selection proceeded.

The selection was performed by constructing likelihood ratios which exploited the full topology of the event. The kinematic variables were chosen on the basis of their internal correlations, which were globally taken into account by the likelihood functions. Events at this stage of the analysis were mostly  $\nu_e$  CC interactions with a genuine primary electron and NC events with an electron from photon conversion or  $\pi^0$  Dalitz decay. In  $\nu_e$  CC events the electron was typically well isolated and balanced the momentum of the hadron jet in the transverse plane. On the other hand, in NC events the electron was embedded in the hadron jet with transverse momentum almost aligned with it. The search for signal had intermediate properties between these two extremes since neutrinos carried away transverse momentum and the sizeable  $\tau$  mass introduced a component of the electron momentum perpendicular to the  $\tau$  direction, thus reducing its isolation.

In order to distinguish the two background sources from the signal, an event classification was implemented with the use of two distinct likelihood functions. The first one was designed to separate signal from NC events and included mainly longitudinal variables. This was motivated by the significant contribution of these variables to the isolation of the electron candidate track. For each event a likelihood ratio  $\lambda_e^{\text{NC}}$  was defined as the ratio of the likelihood functions constructed from signal and NC events, respectively. Likewise  $\lambda_e^{\text{CC}}$  was defined. This second function was designed to distinguish signal from  $\nu_e$  CC events. It included information on the transverse plane kinematics.

The sensitivity was optimized in the plane  $(\ln \lambda_e^{\text{NC}}, \ln \lambda_e^{\text{CC}})$  shown in Figure 9 for simulated signal and backgrounds. A signal region was defined at large values of both  $\ln \lambda_e^{\text{NC}}$  and  $\ln \lambda_e^{\text{CC}}$ . This corresponded to the selection of events where the electron was isolated from the hadron jet but did not balance it in the transverse plane. The optimal sensitivity of the analysis lied in a region characterized by less than 0.5

background events. Data were found to be consistent with background expectations inside the signal region indicated by the boxes in the figure.

In order to optimize the sensitivity to oscillations at low  $\Delta m^2$  an independent analysis was performed with the LM events sample. The condition  $p_H < 1.5 \text{ GeV}/c$  enriched the LM sample in quasielastic (QE) and resonance (RES) events, avoiding double counting with the corresponding DIS search. Overall, the QE and RES events represented 6.3% of the total  $\nu_\mu$  CC interactions. The topology of LM events simplified the reconstruction and the selection criteria in this kinematic region. The prompt electron identification, similar to that used in the DIS search, was applied to primary DC tracks with  $p > 2 \text{ GeV}/c$  and was based on TRD and ECAL information. The background consisted mostly of  $\nu_e$  interactions. Details of the LM analysis are to be found in [10–13].

5.3.  $\tau$  Hadronic Decay Channels. The search for  $\nu_\tau$  appearance was further improved by looking for other decay modes of the  $\tau$  lepton. This was achieved by looking for hadronic decays. Also here two analyses were performed for the DIS and LM samples. We discuss only the DIS analysis. The different hadronic decay modes were treated separately. A muon veto was implemented using both kinematical criteria and particle identification.

The search for  $\tau^- \rightarrow h^-(n\pi^0)\nu_\tau$  decays, where  $h^-$  is a hadron and  $n \geq 0$ , benefited from the large branching ratio of this mode. Two independent analyses of the full inclusive sample were separately optimized for the exclusive  $\tau^- \rightarrow \rho^- \nu_\tau$  and  $\tau^- \rightarrow h^- \nu_\tau$  topologies.

For  $\tau^- \rightarrow \rho^- \nu_\tau$ , the signal search started with the identification of the  $\pi^0$  and  $\pi^-$  candidates produced in the  $\rho^-$  decay. Each of the two photons from  $\pi^0$  decay was detected either as neutral electromagnetic clusters or, in case it converted, as two oppositely charged tracks forming a secondary vertex. Thus, the  $\pi^0$  was searched for either as two separate photons, neutral clusters or conversions, or, in case they coalesce in ECAL, as two overlapped clusters.

In each event all the possible  $\pi^0$  and  $\pi^-$  combinations were considered. A  $\pi^-$  candidate was a DC track with a momentum  $p > 1 \text{ GeV}/c$ . A  $\pi^0 \pi^-$  pair was considered as a  $\rho$  candidate if it had a reconstructed mass  $0.6 < M < 0.9 \text{ GeV}/c^2$ .

Likelihood functions based on the energies of the  $\pi^0$  and of the  $\pi^-$  were defined. Selecting the maximum likelihood combination resulted in the correct choice in about 75% of the cases.

The  $\nu_e$  CC interactions containing bremsstrahlung photons not associated with the electron track could fake the  $\tau \rightarrow \rho$  topology. The electron veto used to reduce this background followed the principles of the muon veto: the highest and second highest  $p_T$  tracks and the  $\pi^-$  candidate were considered candidate electrons. The selection proceeded. The rejection of NC interactions was accomplished by using a likelihood function based on the angles  $\theta_{\nu_T}$  and  $\theta_{\nu_H}$ .

The search was continued with the  $\tau^- \rightarrow h^- \nu_\tau$  channel. The  $h^-$  candidate was the highest  $p_T$  negative primary track, provided it was one of the two highest  $p_T$  tracks of either

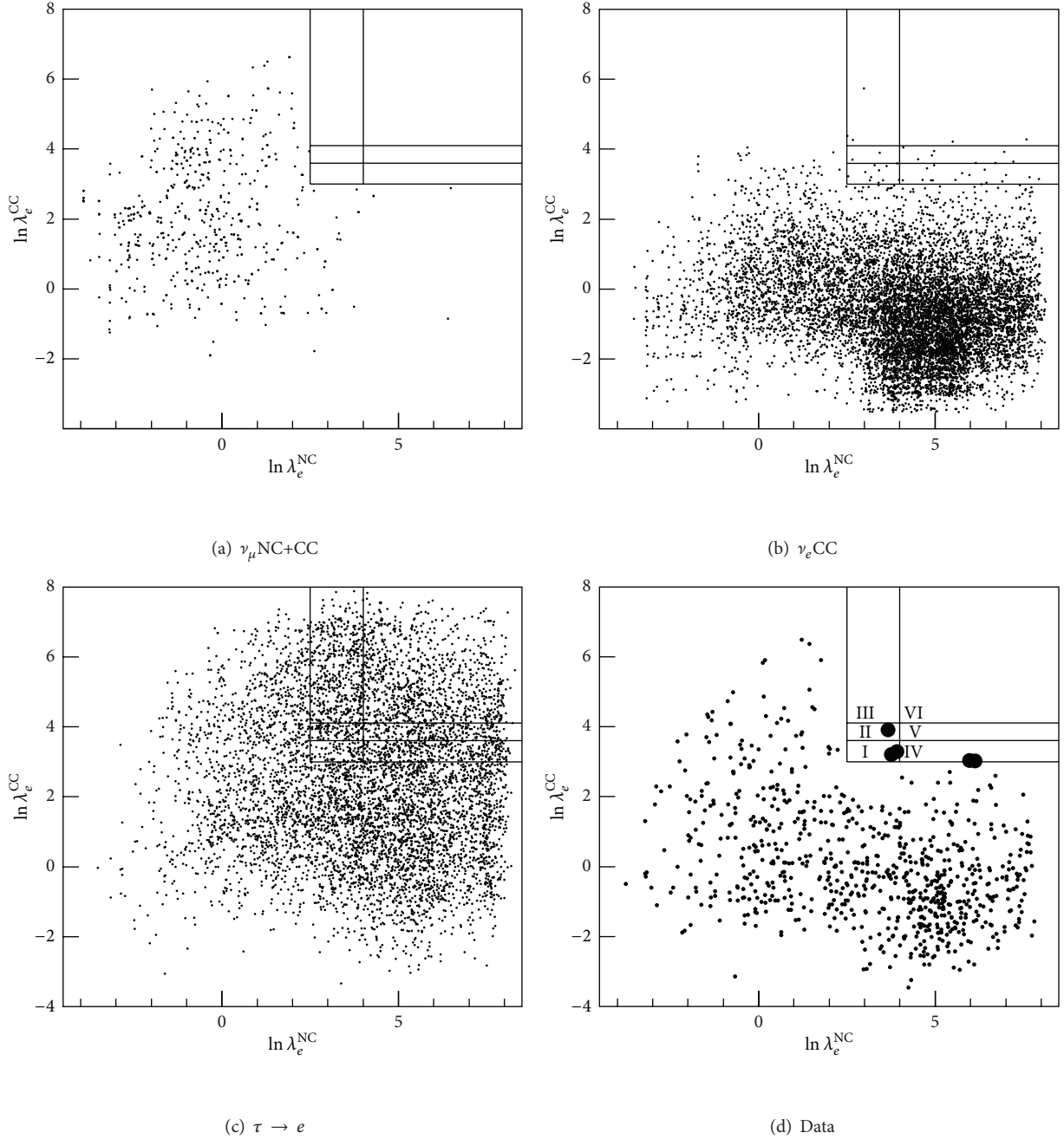


FIGURE 9: Scatter plot of  $\ln \lambda_e^{\text{NC}}$  versus  $\ln \lambda_e^{\text{CC}}$  for simulated signal and backgrounds (from [10–13]). (a) MC  $\nu_\mu$  NC events and the few surviving  $\nu_\mu$  CC events. (b) MC  $\nu_e$  CC events. (c) simulated  $\tau^- \rightarrow e^- \bar{\nu}_e \nu_\tau$  events. (d) data. The box at the upper right corner indicates the signal region and is divided into subboxes for the analysis.

charge in the event. It was then required that this candidate not be identified as a muon or as an electron associated with an energy deposition in the ECAL and that  $3 < p_V^\tau < 150 \text{ GeV}/c$ .

There was a residual background from  $\nu_\mu$  CC interactions in which the outgoing  $\mu$  was selected as the  $h^-$  because it either decayed in flight or suffered a highly inelastic interaction in the calorimeters. This happened in about  $10^{-4}$

of all  $\nu_\mu$  CC events. These events were rejected by a likelihood function.

The study continued with the  $\tau^- \rightarrow h^- h^+ h^- (n\pi^0) \nu_\tau$  decay channel. This channel was characterized by the presence of additional constraints due to the internal  $3h$  structure. This search was optimized for the  $h^- h^+ h^- \nu_\tau$  decay, dominated by the chain  $\tau^- \rightarrow a_1^-(1260) \nu_\tau$ ,  $a_1^- \rightarrow \rho^0(770) \pi^-$ ,  $\rho^0 \rightarrow \pi^+ \pi^-$ . Both the candidate selection and the final background rejection were based upon an artificial neural network (ANN)

technique. The input variables, chosen in order to exploit both the internal structure and the global kinematics of the  $3\pi$  combinations, were the  $3\pi$  invariant mass, the two possible  $\pi^+\pi^-$  invariant masses and  $\theta_{\max}$  and  $\theta_{\min}$ , and the maximum and the minimum opening angles between the three pions. The network was trained on correct and random combinations of the  $\tau$  decay products. The selection of the  $\tau$  daughter candidate as the  $3\pi$  combination with the highest value resulted in the correct choice in 73% of the cases.

The same hadronic decay channels were searched for in the LM topologies [10–13].

**5.4. Conclusion on  $\nu_\mu \nu_\tau$  Oscillation.** The final result of the measurement was expressed as a frequentist confidence interval which accounted for the fact that each  $\tau^-$  decay mode and signal bin may have a different signal to background ratio. The acceptance region became multidimensional to contain each of the separate measurements. This computation took into account the number of observed signal events, the expected background and its uncertainty, and the value of expected signal events if the oscillation probability was unity. For the  $\nu_\mu \rightarrow \nu_\tau$  oscillation this last quantity was defined by

$$N(\nu_\mu \rightarrow \nu_\tau) = N_\mu^{\text{obs}} \cdot \left(\frac{\sigma_\tau}{\sigma_\mu}\right) \cdot \text{Br} \cdot \left(\frac{\varepsilon_\tau}{\varepsilon_\mu}\right), \quad (4)$$

where

- (i)  $N_\mu^{\text{obs}}$  was the observed number of  $\nu_\mu$  CC interactions for the given efficiency  $\varepsilon_\mu$ ;
- (ii)  $\varepsilon_\tau$  and  $\varepsilon_\mu$  were the detection efficiencies for the  $\tau^-$  signal events and  $\nu_\mu$  CC events, respectively. The cuts used to select  $N_\mu^{\text{obs}}$  and  $\varepsilon_\mu$  varied from channel to channel in order to reduce systematic uncertainties in the ratio  $\varepsilon_\tau/\varepsilon_\mu$  for that channel;
- (iii)  $\sigma_\tau/\sigma_\mu$  was the suppression factor of the  $\nu_\tau$  cross-section due to the difference between the  $\tau$  and  $\mu$  masses, which for a given  $\nu_\mu$  spectrum and the large  $\Delta m^2$  hypothesis was evaluated to be 0.48, 0.60, and 0.82 for the DIS, RES, and QE processes;
- (iv) Br was the branching ratio for the considered  $\tau$  decay channel.

The overall systematic uncertainty on the background prediction was estimated to be 20%. The corresponding uncertainty on  $N(\nu_\mu \rightarrow \nu_\tau)$  was 10%. The impact of this latter value on the final combined results was negligible.

The analysis of the full NOMAD data sample gave no evidence for  $\nu_\tau$  appearance. The resulting 90% C.L. upper limit on the two-generation  $\nu_\mu \rightarrow \nu_\tau$  oscillation probability was

$$P(\nu_\mu \rightarrow \nu_\tau) < 2.2 \cdot 10^{-4}. \quad (5)$$

The excluded region in the plane  $(\sin^2 2\theta_{\mu\tau} - \Delta m^2)$  is shown in Figure 10 together with limits published from other experiments [14–18]. In the two-family oscillation formalism

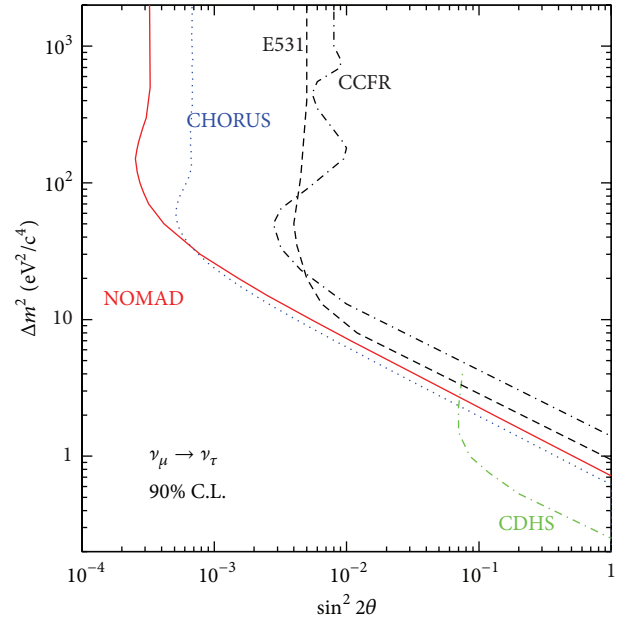


FIGURE 10: Final exclusion plot in the plane  $(\sin^2 2\theta_{\mu\tau} - \Delta m^2)$  for the channel  $\nu_\mu \rightarrow \nu_\tau$ .

this result excludes a region of the  $\nu_\mu \rightarrow \nu_\tau$  oscillation parameters which limits  $\sin^2 2\theta_{\mu\tau}$  at high  $\Delta m^2$  to values smaller than  $3.3 \cdot 10^{-4}$  at 90% CL and  $\Delta m^2$  to values smaller than  $0.7 \text{ eV}^2/c^4$  at  $\sin^2 2\theta_{\mu\tau} = 1$ .

The same analysis can be used to set a limit on  $\nu_e \rightarrow \nu_\tau$  oscillation [19]. As explained before, the beam showed a contamination of  $\nu_e$  at a level of 0.01 compared to  $\nu_\mu$ . Thus, the search of  $\nu_\tau$  appearance gave an excluded region at 90% CL for the  $\nu_e \rightarrow \nu_\tau$  which limits  $\sin^2 2\theta < 1.5 \cdot 10^{-2}$  at large  $\Delta m^2$  and  $\Delta m^2 < 5.9 \text{ eV}^2/c^4$  at  $\sin^2 2\theta = 1$ . For this channel, the sensitivity was not limited by background but by the available statistics. Another oscillation channel was also searched for:  $\nu_\mu \rightarrow \nu_e$ . The result is given in [20].

The NOMAD experiment explored the  $\nu_\mu \rightarrow \nu_\tau$  oscillation channel down to probabilities more than one order of magnitude smaller than limits set by the previous generation of experiments. For the first time a purely kinematical approach was applied to the detection of  $\nu_\tau$  CC interactions. This demonstrated that the approach developed into a mature technique. Unfortunately, oscillations were not discovered with the NOMAD experiment; the neutrino masses found in subsequent experiments proved to be much too small to contribute significantly to the missing mass of the Universe, although it is known today that neutrinos account for a part about as large as the one due to all the stars present in the Universe.

## 6. Study of Strange Particle Production in $\nu_\mu$ CC Interactions

A number of NOMAD publications dealt with strangeness production in neutrino interactions [9, 21–25]. We present some of these results.

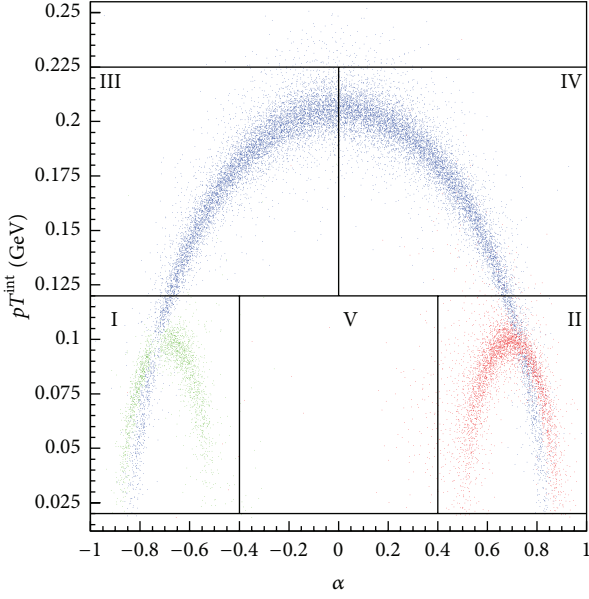


FIGURE 11: Plot of  $p_T^{\text{int}}$  versus  $\alpha$  identifying the populations of strange particles (from [22]).  $\bar{\Lambda}$ 's and  $\Lambda$ 's populate boxes I and II, respectively. The  $K_s^0$  sample being symmetric is found in all boxes except box V. Photon conversions populate the small  $p_T^{\text{int}}$  region.

**6.1. Yields of Strange Particles [9].** The production of strange particles in neutrino interactions provided a testing ground for the quark-parton and for hadronization models. Neutral strange particles could be reliably identified using the  $V^0$ -like signature of their decays in contrast to most other hadrons which require particle identification hardware. All previous investigation of strange particle production by neutrinos came from bubble chamber experiments which suffered from low statistics. Most recent references are given in [26–28].

Among the  $1.3 \cdot 10^6$   $\nu_\mu$  CC events collected, the NOMAD experiment observed an unprecedented number of neutral particle decays appearing as a  $V^0$ -like vertex in the detector with an excellent reconstruction quality. The order of magnitude increase in statistics was used to improve our knowledge of  $K_s$ ,  $\Lambda$ ,  $K^{*\pm}$ ,  $\Sigma^{*\pm}$ ,  $\Xi^-$ , and  $\Sigma^0$  production in  $\nu_\mu$  CC interactions. This study allowed a quantitative theoretical interpretation of the  $\Lambda$  polarization measurements as will be discussed later.

Since NOMAD was unable to distinguish protons from pions in the momentum range of the analysis, the  $V^0$  identification procedure relied on the kinematic properties of the  $V^0$  decay. The fit method was performed for three decay hypotheses,  $K_s \rightarrow \pi^+\pi^-$ ,  $\Lambda \rightarrow p\pi^-$ , and  $\bar{\Lambda} \rightarrow \bar{p}\pi^+$ , and for the hypothesis of a gamma conversion to  $e^+e^-$ .

Figure 11 shows the plot  $p_T^{\text{int}}$  versus  $\alpha$  in data events, where  $p_T^{\text{int}}$  is the transverse component of one of the outgoing charged tracks with respect to the  $V^0$  momentum and  $\alpha = (p_L^+ - p_L^-)/(p_L^+ + p_L^-)$  is the longitudinal momentum asymmetry between the positive and negative tracks.

Different regions of the plot correspond to different populations. Three regions corresponding to  $K_s^0$ ,  $\Lambda$ , and  $\bar{\Lambda}$  are

clearly visible, with the  $K_s^0$  sample being symmetric. Identified  $V^0$  were of two types:

- (i) uniquely identified  $V^0$ , which populated regions in which decays of only a single particle type were present;
- (ii) ambiguously identified  $V^0$  which populated regions in which decays of different particle types were present.

It was possible to select subsamples of uniquely identified  $V^0$ 's with high purity: 98% for  $K_s^0$ , 97% for  $\Lambda$ , and 90% for  $\bar{\Lambda}$ .

The treatment of ambiguities aimed at selecting a given  $V^0$  decay with the highest efficiency and the lowest background contamination from other  $V^0$  types. MC was used to define the criteria for the kinematic  $V^0$  selection and to determine the purity of the final samples. Samples consisting of more than 90% of uniquely identified  $V^0$  were selected.

The total  $V^0$  sample contained 15074 identified  $K_s$ , 8987 identified  $\Lambda$ , and 649 identified  $\bar{\Lambda}$ , representing significantly larger numbers than in previous experiments performed with bubble chambers. Thus the production rate of neutral strange particles in  $\nu_\mu$  CC interactions was measured. The integral yields per  $\nu_\mu$  CC interactions were the following:

$$\begin{aligned}
 (6.76 \pm 0.06) \% & \quad \text{for } K_s, \\
 (5.04 \pm 0.06) \% & \quad \text{for } \Lambda, \\
 (0.37 \pm 0.02) \% & \quad \text{for } \bar{\Lambda}.
 \end{aligned} \tag{6}$$

The yields of  $K_s$  rose steadily with  $E_\nu$  and  $W^2$  reached a plateau at large  $Q^2$  and fell with increasing Bjorken scaling variable  $x_{Bj}$ . The  $\Lambda$  yield showed a behavior almost independent of  $E_\nu$ ,  $W^2$ , and  $Q^2$  after a sharp initial rise. The  $\bar{\Lambda}$  yields were measured for the first time. All the plots appear in [9].

Furthermore, a detailed analysis of kinematic quantities describing the behavior of neutral strange particles inside the hadronic jet was performed. In particular, the following distributions were studied:

- (i) the Feynman- $x$ , the longitudinal momentum fraction in the hadronic center of mass system,  $x_F = 2p_L^*/W$ ;
- (ii) the fraction  $z = E_{\text{lab}}(V^0)/E_{\text{lab}}$  (all hadrons) of the hadronic energy carried away by the neutral strange particle in the laboratory system;
- (iii) the transverse momentum squared  $p_T^2$ , of a particle with respect to the hadronic jet direction.

The  $x_F$  distribution indicated that  $\Lambda$ 's were produced mainly in the target fragmentation region ( $x_F < 0$ ) while  $K_s$  were peaked in the central region with an asymmetry in the forward direction.  $\bar{\Lambda}$ 's were produced in the central  $x_F$  region ( $-0.5 < x_F < 0.5$ ).

The  $z$  distributions showed a turnover at small values of  $z$  for  $\bar{\Lambda}$  but not for  $K_s^0$  and  $\Lambda$  which showed a maximum at  $z \rightarrow 0$ .

The  $p_T^2$  distributions showed an exponential behavior of the form  $\exp(-Bp_T^2)$  with a slope parameter  $B$  in the region  $0 < p_T^2 < 0.5 \text{ GeV}^2/c^2$  around 5.7 for  $K_s^0$ , 4.4 for  $\Lambda$ , and 3.9 for  $\bar{\Lambda}$ .

**6.2. Measurement of the  $\Lambda$  Polarization [23, 24].** The study of  $\Lambda$  polarization relied on an efficient and robust  $\Lambda$  hyperon identification algorithm and a high statistics sample.  $\Lambda$  hyperons were identified via their decay  $\Lambda \rightarrow p\pi^-$ . As discussed above, the identification procedure optimized both the selection efficiency and the purity of the final sample. It required the presence of an identified muon at the primary vertex, both primary and  $V^0$  vertices in the fiducial volume and a reconstructed energy  $E_\nu < 450 \text{ GeV}$ . Samples of 8987  $\Lambda$ 's and 649  $\bar{\Lambda}$ 's were selected with global efficiencies of  $(16.4 \pm 0.1)\%$  and  $(18.6 \pm 0.5)\%$  corresponding to purities of  $(95.9 \pm 0.1)\%$  and  $(89.7 \pm 0.7)\%$ , respectively.

The  $\Lambda$  polarization was measured by the asymmetry in the angular distribution of the proton. In the  $\Lambda$  rest frame the decay protons are distributed as follows:

$$\frac{1}{N} \frac{dN}{d\Omega} = \left( \frac{1}{4\pi} \right) (1 + \alpha_\Lambda \mathbf{P} \cdot \mathbf{k}), \quad (7)$$

where  $\mathbf{P}$  is the  $\Lambda$  polarization vector,  $\alpha_\Lambda = (0.642 \pm 0.013)$  is the decay asymmetry parameter, and  $\mathbf{k}$  is the unit vector along the decay direction of the positive track.

Dependences of the polarization on  $x_F$ ,  $W^2$ ,  $Q^2$ , and  $p_T$  were studied together with the target nucleon type (neutrons or protons). This is discussed in [23, 24]. Negative polarizations along the  $W$ -boson direction ( $P_x$ ) and in the direction orthogonal to the production plane ( $P_y$ ) were found. This was the first time that a neutrino experiment observed a nonzero transverse polarization  $P_y$ . The longitudinal polarization showed an enhancement in the target fragmentation region ( $x_F < 0$ ):  $P_x = -0.21 \pm 0.04(\text{stat}) \pm 0.02(\text{sys})$ , while in the current fragmentation region ( $x_F > 0$ ) the longitudinal polarization was found to be  $P_x = -0.09 \pm 0.06(\text{stat}) \pm 0.03(\text{sys})$ . A similar dependence on  $x_F$  was observed for the transverse polarization.

There was an enhancement of the longitudinal polarization in both low  $W^2$  ( $< 15 \text{ GeV}^2$ ) and low  $Q^2$  ( $< 5 \text{ GeV}^2$ ) regions. Both  $P_x$  and  $P_y$  strongly depend on the  $p_T$  of the  $\Lambda$  with respect to the hadronic jet direction, in qualitative agreement with the results of unpolarized hadron-hadron measurements.

The longitudinal polarization in the proton-like target sample was found to be negative and enhanced in comparison with the total event sample. This could be interpreted as being due to  $\Lambda$ 's coming from the decay of  $\Sigma^{*+}$  and other heavier baryons. The measured longitudinal polarization in the neutron-like target sample was also negative and probably more directly related to the polarized strange content of the nucleon. The transverse polarization was more evident in the neutron-like sample where most  $\Lambda$ 's were produced promptly.

The  $\bar{\Lambda}$  polarization was also measured. The results are given in [25].

## 7. Dimuon Charm Production

The most recent NOMAD publication [29] concerns the dimuon charm production in neutrino interactions.

The process of charm dimuon production stems from the  $\nu_\mu$  CC production of a charm quark which semileptonically decays into a final-state secondary muon with its electric charge opposite to that of the muon from the leptonic CC vertex. The DIS production of charm quarks involves the scattering off strange and nonstrange quark contents of the nucleon. However the contributions from  $u$ - and  $d$ -quarks are suppressed by the small quark-mixing matrix elements.

The signal consists in two muons of opposite sign coming from a common vertex. A measurement of the cross-section for charm dimuon production in neutrino DIS off nucleons provides the most direct and clean probe of  $s$ , the strange quark sea content of the nucleon. Traditionally charm dimuon production in neutrino interactions was measured in massive calorimeters in order to obtain a sizable number of events [30–37]. Because of its lowest energy threshold,  $E_\nu \sim 6 \text{ GeV}$ , and its high resolution, NOMAD reached a new level of precision in this measurement. Furthermore, the neutrino spectrum in NOMAD was well suited to study charm production close to the charm threshold, providing enhanced sensitivity to the charm production parameters.

**7.1. Dimuon Selection.** The FCAL was used as the interaction target to profit from its large mass. The selection of the events required a deposition of energy in the FCAL of more than 3.5 m.i.p., together with the  $V_8$  veto and two muons accurately analysed in the DC region and well recognized in the muon system. Such a signal selected opposite sign dimuons and like-sign dimuons which gave a direct estimate of the background.

The total hadronic energy was calculated with both the energy measured in the FCAL and the energies measured in the DC's with the proper corrections included.

The selection was based on a primary muon (the highest energy one) of negative charge, thus suppressing the contribution of antineutrino interactions.

**7.2. Charm Dimuon Results.** The charm dimuon events were determined from the opposite sign dimuon signal measured in the data after subtracting the background coming from muonic decays of hadrons in the hadronic shower:

$$N_{\mu\mu^c} = N_{\mu\mu^+} - N_{\mu\mu^{+bg}}. \quad (8)$$

The background was evaluated from the  $\mu^-\mu^-$  events corrected by a scale factor extracted from the MC. The background estimate was checked using the data themselves consisting in mesons of both charges detected in the DC's.

After all cuts, the analysis retained 20479 opposite sign dimuons of which 75% were genuine charm signals. This represented the highest available statistics, and the quality of the reconstruction allowed to lower significantly the energy threshold on the second muon down to 3 GeV. This feature gave an additional sensitivity to evaluate the charm production parameters.

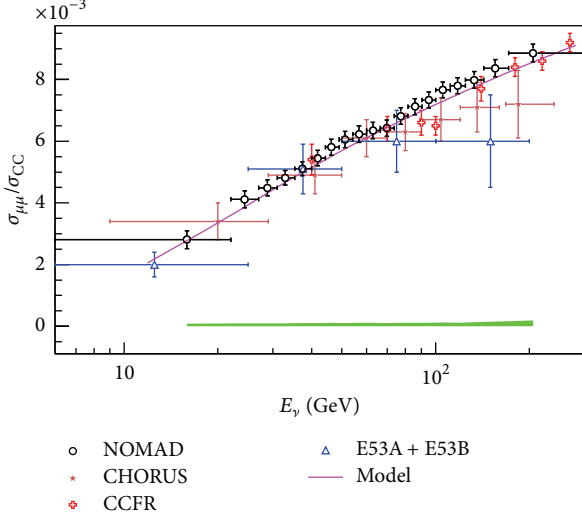


FIGURE 12: Ratio between charm dimuon cross-section and inclusive  $\nu_\mu$  CC cross-section from NOMAD (from [29]). Previous measurements are also shown.

The analysis measured the ratio of the charm dimuon cross-section to the inclusive CC cross-section as a function of the kinematic variables:

$$R_{\mu\mu} = \frac{\sigma_{\mu\mu}}{\sigma_{CC}} \equiv \frac{N_{\mu\mu c}}{N_{CC}}. \quad (9)$$

The final result for  $R_{\mu\mu}$ , shown as a function of the neutrino energy, is given in Figure 12.

By integrating this result, the average dimuon production in NOMAD was evaluated. Over the NOMAD flux, for  $Q^2 \geq 1 \text{ GeV}^2/c^2$ , the result was  $(5.15 \pm 0.05 \pm 0.07) 10^{-3}$ . The first uncertainty is statistical and the second systematic.

Fitting  $R_{\mu\mu}$  allowed to extract the charm production parameters including the mass of the charm quark  $m_c$ , the effective semileptonic branching ratio  $B_\mu$ , and the strange sea suppression factor.

The running mass of the charm quark, evaluated in the  $\overline{MS}$  scheme, was found to be

$$m_c = (1.159 \pm 0.075) \text{ GeV}/c^2. \quad (10)$$

The semileptonic branching ratio was parameterized as a function of the neutrino energy:

$$B_\mu(E_\nu) = \frac{(0.097 \pm 0.003)}{\{1 + (6.7 \pm 1.8 \text{ GeV})/E_\nu\}}. \quad (11)$$

The strange quark sea suppression factor was found to be

$$\kappa_s = 0.591 \pm 0.019 \quad \text{at } Q^2 = 20 \text{ GeV}^2/c^2. \quad (12)$$

These results represent the most precise measurements from neutrino data.

## 8. Other Physics Topics

The NOMAD experiment conducted several other measurements: inclusive production of resonances [38], Bose-Einstein correlations in  $\nu_\mu$  CC interactions [39],  $\nu_\mu$ -nucleon

cross-section off an isoscalar target [40], study of quasielastic events [41], coherent neutral pion production [42], single photon production [43], and backward going particles [44]. Also some more exotic ideas were tested: search for a new gauge boson [45], search for eV scalar penetrating particles [46], and search for heavy neutrinos [47]. We will develop some of these topics.

**8.1. Inclusive Production of Various Resonances [38].** NOMAD measured the production yield of meson resonances  $\rho^0(770)$ ,  $f_0(980)$ , and  $f_2(1270)$ . In particular the  $f_0$  meson was observed for the first time in neutrino interactions. All combinations of tracks with momenta larger than  $0.1 \text{ GeV}/c$  originating at the primary vertex and not identified as electrons or muons were used for the reconstruction of the resonance candidates. All used tracks were assigned the pion mass.

The distribution of the  $\pi^+\pi^-$  invariant mass showed an enhancement at the  $\rho^0$  mass which was not present in the like-sign distributions. When a cut  $x_F > 0.6$  was applied to reduce the combinatorial background, clear peaks at the  $f_0$  and  $f_2$  masses were visible. The result is shown in Figure 13. The resonance signal was determined by fitting the invariant mass distribution to a sum of relativistic Breit-Wigner functions with combinatorial background added.

The average  $\rho^0(770)$  multiplicity measured for  $\nu_\mu$  CC interactions was found to be  $(0.195 \pm 0.007 \pm 0.019)$  for  $W > 2 \text{ GeV}$ . It was found to be the same in  $\bar{\nu}_\mu$  CC interactions.

NOMAD also measured the production of strange resonances and heavier hyperons. This study was of interest to tune the LUND model parameters and for the theoretical interpretation of  $\Lambda$  and  $\bar{\Lambda}$  polarization measurements. This was essential because  $\Lambda$ 's originating from the decays of  $\Sigma^*$ ,  $\Sigma^0$ , and  $\Xi$  inherit a polarization from their parent particles different from that of a directly produced  $\Lambda$ .

To construct the samples, neutral strange particles were combined with all possible charged tracks of appropriate sign emerging from the primary vertex except those identified as muons or electrons. Combinations of  $\Lambda$  with  $\gamma$  were also studied, where photons were identified as conversions in the detector fiducial volume.

The  $K^{*\pm}$  was recognized in the  $K_s\pi^\pm$  invariant mass distributions and the  $\Sigma^{*\pm}$  appeared in the  $\Lambda\pi^\pm$  combinations. Still in the  $\Lambda\pi^-$  there was evidence of  $\Xi^-$  production.  $\Xi^0$  showed in the invariant mass distribution of  $\Lambda\gamma$  combinations. All these plots appear in [9, 38].

Corrected fractions of observed  $K_s^0$  and  $\Lambda$  decays that originate from the decays of strange resonances and heavy hyperons were found to be  $(15.5 \pm 0.9)\%$ ,  $(8.7 \pm 0.7)\%$ ,  $(5.8 \pm 1.1)\%$ ,  $(2.6 \pm 0.8)\%$ ,  $(7.3 \pm 2.4)\%$ , and  $(1.9 \pm 1.7)\%$  for the channels  $K^{*+} \rightarrow K_s^0\pi^+$ ,  $K^{*-} \rightarrow K_s^0\pi^-$ ,  $\Sigma^{*+} \rightarrow \Lambda\pi^+$ ,  $\Sigma^{*-} \rightarrow \Lambda\pi^-$ ,  $\Sigma^0 \rightarrow \Lambda\gamma$ , and  $\Xi^- \rightarrow \Lambda\pi^-$ , respectively.

**8.2. Study of Quasielastic Events [41].** With its high granularity target NOMAD was well suited to study the  $\nu_\mu$  quasielastic scattering reaction (QEL):  $\nu_\mu n \rightarrow \mu^- p$ . The data sample used in this analysis consisted of 751000  $\nu_\mu$  CC events in a reduced fiducial volume, the average energy of the incoming  $\nu_\mu$  being

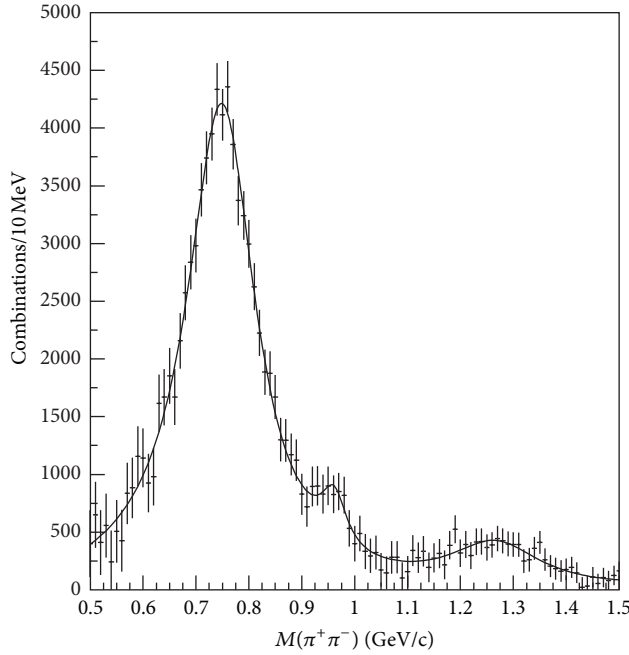


FIGURE 13: Distribution of the  $\pi^+\pi^-$  invariant mass showing evidences for  $\rho^0(770)$ ,  $f_0(980)$ , and  $f_2(1270)$  production after background suppression.

25 GeV. Previous data came mostly from bubble chamber experiments and suffered from small statistics. Moreover large systematic uncertainties came from the poor knowledge of the incoming neutrino flux. For some previous results, see [48–50].

The event selection retained two tracks originating from the primary vertex, one of them identified as a muon. The muon track was easily reconstructed; however the proton was more difficult to measure. Sometimes the proton could not be reconstructed because its momentum was too low, well below 1 GeV/c, or its angle too large, above 60 degrees. For positive tracks such conditions meant that they made almost immediately a  $U$ -turn due to the magnetic field. Positive particles were deviated upwards so that their trajectories ended almost parallel to the DC planes. It was crucial to choose a region in the detector with a stable reconstruction efficiency. This was achieved by selecting QEL events where protons were emitted in the lower hemisphere of the detector. Consequently a cut selected muons in the upper hemisphere.

Moreover the tracks were in the  $1/\beta^2$  region of ionization loss and they crossed the drift cells at very large angles where the spatial resolution of the DC was considerably worse. Some of these effects were difficult to parameterize and simulate. Also the proton could lose part of its energy in an intranuclear cascade. In the analysis it was important to disentangle the reconstruction efficiency effects from the effects induced by intranuclear cascade which changed the proton kinematics.

Using only 2-track events did not alleviate the problem of a large systematic uncertainty coming from insufficient understanding of nuclear effects. So the 1-track sample, muon only, was also used. For these events the muon momentum

and direction were the sole measurements and conservation laws were used to compute other kinematical quantities like  $E_\nu$  and  $Q^2$ . The expected ratio between 1-track and 2-track events for QEL was calculated to be 54%–46%.

In total the samples used in the analysis consisted of 14021 neutrino and 2237 antineutrino events. No precise knowledge of the integrated neutrino flux existed, so the QEL cross-section was normalized to the total DIS  $\nu_\mu$  CC cross-section or to inverse muon decay.

The flux-averaged QEL cross-section was measured in the neutrino energy region 3–100 GeV. The result for  $\nu_\mu$  was

$$\sigma_{\text{QEL}} = (0.92 \pm 0.02 \text{ (stat)} \pm 0.06 \text{ (syst)}) \cdot 10^{-38} \text{ cm}^2 \quad (13)$$

and for the antineutrino case

$$\sigma_{\text{QEL}} = (0.81 \pm 0.05 \text{ (stat)} \pm 0.09 \text{ (syst)}) \cdot 10^{-38} \text{ cm}^2. \quad (14)$$

The cross-section depends on the axial form factor  $F_A(Q^2)$  of the nucleon which is parameterized with only one adjustable parameter, the so-called axial mass  $M_A$ . This parameter describes the internal structure of the nucleon and should be the same for both neutrino and antineutrino measurements. The conventional representation uses the form:  $F_A(Q^2) = F_A(0)(1+Q^2/M_A^2)^{-2}$ , where  $F_A(0) = -1.2695 \pm 0.0029$  comes from neutron  $\beta$ -decay.

With the neutrino data the result was  $M_A = 1.05 \pm 0.02 \text{ (stat)} \pm 0.06 \text{ (syst)}$  GeV and with the antineutrino  $M_A = 1.06 \pm 0.07 \text{ (stat)} \pm 0.12 \text{ (syst)}$  GeV.

**8.3. Backward Going Particles [44].** In high energy interactions off nuclei there are particles emitted backwards with respect to the beam direction which have energies not allowed by the kinematics of collisions on a free and stationary nucleon. Backward going protons are commonly observed while, in absence of nuclear effects, their production is forbidden. Likewise, high energy mesons are detected at momenta above the kinematical limit. These effects have been used to investigate nuclear structure. Two categories of models are proposed to explain the origin of these particles.

- (i) In the intranuclear cascade models, the production of particles in the kinematically forbidden region can be seen as the result of multiple scattering and of interactions of secondary hadrons produced in the primary  $\nu$ -nucleon collision, while they propagate through the nucleus. One observes that the cascade is restricted to slow particles only, while the fast ones do not reinteract inside the nucleus. The currently accepted explanation for this effect is the “formation zone” concept. This is the distance from the production point which is required for the secondary hadrons to be “formed” and be able to interact as physical hadronic states. An advantage of neutrino-induced interactions with respect to hadronic processes is the fact that the projectile interacts only once.
- (ii) In the correlated nucleon/quark models the backward particles are produced in the collisions off structures with mass larger than the mass of the nucleon. These

structures are formed under the action of the short-range part of the nuclear force; they represent the effects of gathering two or more nucleons in small volumes.

The full NOMAD sample of  $\nu_\mu$  CC events having a muon momentum of at least 3 GeV/c used in this analysis amounted to 944000 events. Only tracks attached to the primary vertex and having at least 8 DC hits were used in the search for backward particles. The separation between backward protons and pions was done on plots showing length versus momentum tracks. Protons were only visible in the plot of positive tracks having a relatively small length. With the help of MC simulations corrections were applied for reconstruction, stopping, and identification efficiencies. The contamination of pions in the sample of identified protons amounted to 8% above 250 MeV/c.

The average number of backward protons per event was found to be around 5%. The rates were studied as a function of the hadronic energy  $E_{\text{had}}$  and of  $Q^2$ . A decrease of the yield with increasing  $E_{\text{had}}$  and  $Q^2$  was observed.

The slope parameter  $B$  of the invariant cross-section, parameterized as  $\exp(-Bp^2)$ , has been measured and found to be consistent with previous  $\nu$ -nucleus and hadron-nucleus experiments.  $B$  was found not to depend on  $E_{\text{had}}$  and  $Q^2$  over a wide range of values. Its value was  $B \sim 10 \text{ c}^2/\text{GeV}^2$ . This was in agreement with “nuclear scaling” previously observed in hadronic experiments.

The backward proton rate measured in the NOMAD target (mainly carbon) has been compared with the values obtained on different nuclei. While the  $A$  dependence for neutrino scattering on heavy nuclei is consistent with that of hadron experiments and can be parameterized as  $A^\alpha$  with  $\alpha = 0.68$ , the NOMAD result does not fit this dependence. The  $A$  dependence of backward pions was found to be steeper than that of backward protons.

The backward proton data was compared with the predictions of reinteractions and short-range models. The observed energy dependence is consistent with the “formation zone” mechanism. The correlation between the multiplicity of slow tracks and backward protons indicates the effects of reinteractions.

**8.4. Search for Heavy Neutrinos [47].** The existence of sterile neutrinos has been advocated to explain several experimental anomalies. Many models that attempt to unify the presently known interactions into a single gauge scheme predict such heavy neutrinos which are decoupled from  $W$  and  $Z$  bosons. They are also predicted in extended electroweak and see-saw models trying to solve the problem of baryo- or leptogenesis in the Universe. Stringent experimental limits were published on mixings with  $\nu_e$  and  $\nu_\mu$  [51, 52]. NOMAD allowed a test of a neutral heavy lepton ( $\nu_4$ ) dominantly associated with the  $\nu_\tau$  via the mixing term  $U_{\tau 4}^2$ .

In this search the potential source of  $\nu_4$  was  $D_s$  produced at the proton target and decaying via  $D_s \rightarrow \tau\nu_4$ . As a consequence, the search was limited to  $\nu_4$  masses smaller than 190 MeV/c<sup>2</sup>. If  $\nu_4$  was a long-lived particle, its flux

would penetrate the downstream shielding without significant attenuation. For masses below the  $\pi^0$  mass, the dominant heavy neutrino visible decay in the detector would be  $\nu_4 \rightarrow \nu_\tau e^+ e^-$  with a rate given by the weak interaction diagrams. It would appear as an excess of isolated  $e^+ e^-$  pairs above those expected from standard interactions. The experimental signature of these events was clean and they could be selected with small background due to the excellent capability for precise measurement of the  $e^+ e^-$  pair direction in NOMAD.

With the above hypotheses, the  $\nu_4$  flux and the consequent  $e^+ e^-$  spectrum were calculated. The search used the full data sample. The strategy consisted of identifying  $e^+ e^-$  candidates by reconstructing isolated low invariant mass  $e^+ e^-$  pairs in the DC target that were accompanied by no other activity in the detector. At least one of the two tracks had to be identified as an electron in the TRD, no  $\gamma$  in the ECAL and an HCAL energy smaller than 400 MeV, and  $e^+ e^-$  invariant mass smaller than 95 MeV/c<sup>2</sup>. Only 207 events passed the criteria. A collinearity variable was used to select events with a small angle between the average neutrino beam direction and the total momentum of the reconstructed  $e^+ e^-$  pair. A cut on this angle allowed a very effective background suppression. Checks of the procedure were done using a  $\nu_\mu$  CC data sample with  $e^+ e^-$  pairs from photons converted in the DC target at a large distance from the primary vertex. MC simulations were used to correct the data for acceptance losses, experimental resolution and reconstruction efficiencies. Checks were performed in order to verify the reliability of the simulation using reconstructed  $\pi^0$ 's with one photon converted in the DC.

The largest contribution to the background was expected from neutrino interactions yielding a single  $\pi^0$  with little hadronic activity in the final state. A blind analysis resulted in one event passing the selection criteria, consistent with the expected background and hence no evidence for isosinglet neutrino decays was found. This allowed a 90% CL upper limit on the corresponding mixing amplitude  $U_{\tau 4}^2$  in the  $(m_4, U_{\tau 4}^2)$  plane. The limit reached  $10^{-3}$  for a mass  $m_4$  of 140 MeV/c<sup>2</sup>.

## 9. Conclusion

The NOMAD experiment did not discover neutrino oscillations. We know now that the masses of the neutrino states are much smaller than the 1 eV level originally hoped for in the experiment. This means that cosmological neutrinos cannot contribute predominantly to the intriguing problem of the missing mass found in the Universe. Nevertheless, NOMAD put limits on the  $\nu_\mu \rightarrow \nu_\tau$  oscillation channel that are two orders of magnitude better than previous published limits, and this result remains 15 years later.

Furthermore, because of its high spatial resolution and identification capabilities, the experiment contributed to a deeper understanding of neutrino properties measuring many other standard processes and testing several theoretical suggestions. The list of publications gives a summary of all the topics which have been studied by the experiment. In this paper we have shown a selection of the obtained results.

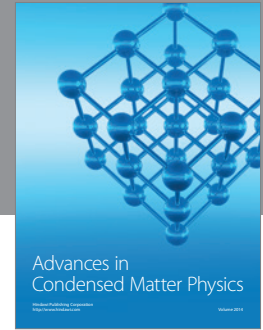
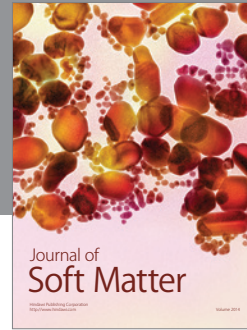
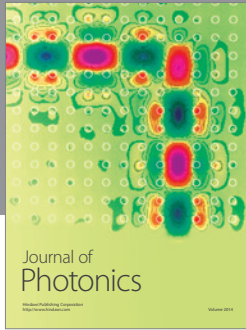
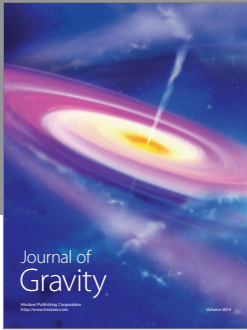
## Conflict of Interests

The author declares that there is no conflict of interests regarding the publication of this paper.

## References

- [1] P. Astier, D. Autiero, A. Baldisseri et al., “Prediction of neutrino fluxes in the NOMAD experiment,” *Nuclear Instruments and Methods in Physics Research A*, vol. 515, no. 3, pp. 800–828, 2003.
- [2] M. Anfreville, P. Astier, M. Authier et al., “The drift chambers of the NOMAD experiment,” *Nuclear Instruments and Methods in Physics Research A*, vol. 481, no. 1–3, pp. 339–364, 2002.
- [3] J. Altegoer, M. Anfreville, C. Angelini et al., “The NOMAD experiment at the CERN SPS,” *Nuclear Instruments and Methods in Physics Research A*, vol. 404, no. 1, pp. 96–128, 1998.
- [4] G. Bassompierre, M. Bermond, M. Berthet et al., “A large area transition radiation detector for the NOMAD experiment,” *Nuclear Instruments and Methods in Physics Research A*, vol. 403, pp. 363–382, 1998.
- [5] G. Bassompierre, S. Bunyatov, T. Fazio et al., “Performance of the NOMAD transition radiation detector,” *Nuclear Instruments and Methods in Physics Research A*, vol. 411, pp. 63–74, 1998.
- [6] D. Autiero, M. Baldo-Ceolin, G. Barichello et al., “The electromagnetic calorimeter of the NOMAD experiment,” *Nuclear Instruments and Methods in Physics Research A*, vol. 373, pp. 358–373, 1996.
- [7] D. Autiero, M. Baldo-Ceolin, F. Bobisut et al., “A study of the transverse fluctuations of hadronic showers in the NOMAD electromagnetic calorimeter,” *Nuclear Instruments and Methods in Physics Research A*, vol. 411, no. 2–3, pp. 285–303, 1998.
- [8] J. Altegoer, J. Andrlé, S. Boyd et al., “The trigger system of the NOMAD experiment,” *Nuclear Instruments and Methods in Physics Research A*, vol. 428, no. 2–3, pp. 299–316, 1999.
- [9] P. Astier, D. Autiero, A. Baldisseri et al., “A study of strange particle production in  $\nu_\mu$  charged current interactions in the NOMAD experiment,” *Nuclear Physics B*, vol. 621, no. 1–2, pp. 3–34, 2002.
- [10] J. Altegoer, C. Angelini, P. Astier et al., “A search for  $\nu_\mu \rightarrow \nu_\tau$  oscillations using the NOMAD detector,” *Physics Letters B*, vol. 431, no. 1–2, pp. 219–236, 1998.
- [11] P. Astier, D. Autiero, A. Baldisseri et al., “A more sensitive search for  $\nu_\mu \rightarrow \nu_\tau$  oscillations in NOMAD,” *Physics Letters B*, vol. 453, no. 2–3, pp. 169–186, 1999.
- [12] P. Astier, D. Autiero, A. Baldisseri et al., “Updated results from the  $\nu_\tau$  appearance search in NOMAD,” *Physics Letters B*, vol. 483, no. 4, pp. 387–404, 2000.
- [13] P. Astier, D. Autiero, A. Baldisseri et al., “Final NOMAD results on  $\nu_\mu \rightarrow \nu_\tau$  and  $\nu_e \rightarrow \nu_\tau$  oscillations including a new search for  $V_\tau$  appearance using hadronic  $\tau$  decays,” *Nuclear Physics B*, vol. 611, no. 1–3, pp. 3–39, 2001.
- [14] T. Kondo, N. Ushida, S. Tasaka et al., “Limits to  $\nu_\mu, \nu_e \rightarrow \nu_\tau$  oscillations and  $\nu_\mu, \nu_e \rightarrow \tau^-$  direct coupling,” *Physical Review Letters*, vol. 57, no. 23, pp. 2897–2900, 1986.
- [15] E. Eskut, A. Kayis, G. Onengüt et al., “A search for  $\nu_\mu \rightarrow \nu_\tau$  oscillation,” *Physics Letters B*, vol. 424, no. 1–2, pp. 202–212, 1998.
- [16] M. Gruwé, C. Mommaert, P. Vilain et al., “Search for  $\nu_\mu \rightarrow \nu_\tau$  oscillation,” *Physics Letters B*, vol. 309, no. 3–4, pp. 463–468, 1993.
- [17] K. S. McFarland, G. J. Feldman, C. Guyot et al., “A search for  $\nu_\mu$  oscillations in the  $\Delta m^2$  range 0.3–90 eV<sup>2</sup>,” *Physics Letters B*, vol. 134, no. 3–4, pp. 281–286, 1984.
- [18] F. Dydak, T. Kondo, S. Tasaka et al., “Limits to  $\nu_\mu, \nu_e \rightarrow \nu_\tau$  oscillations and  $\nu_\mu, \nu_e \rightarrow \tau^-$  direct coupling,” *Physical Review Letters*, vol. 57, no. 23, pp. 2897–2900, 1986.
- [19] P. Astier, D. Autiero, A. Baldisseri et al., “Limit on  $\nu_e \rightarrow \nu_\tau$  oscillations from the NOMAD experiment,” *Physics Letters B*, vol. 471, no. 4, pp. 406–410, 2000.
- [20] P. Astier, D. Autiero, A. Baldisseri et al., “Search for  $\nu_\mu \rightarrow \nu_e$  oscillations in the NOMAD experiment,” *Physics Letters B*, vol. 570, no. 1–2, pp. 19–31, 2003.
- [21] D. Naumov, A. Chukanov, E. Naumova et al., “A study of strange particles produced in neutrino neutral current interactions in the NOMAD experiment,” *Nuclear Physics B*, vol. 700, no. 1–3, pp. 51–68, 2004.
- [22] A. Chukanov, D. Naumov, B. Popov et al., “Production properties of  $K^*(892)^\pm$  vector mesons and their spin alignment as measured in the NOMAD experiment,” *The European Physical Journal C*, vol. 46, no. 1, pp. 69–79, 2006.
- [23] P. Astier, D. Autiero, A. Baldisseri et al., “Measurement of the  $\bar{\lambda}$  polarization in  $\nu_\mu$  charged current interactions in the NOMAD experiment,” *Nuclear Physics B*, vol. 588, no. 1–2, pp. 3–36, 2000.
- [24] B. A. Popov, “Measurement of the  $\Lambda$  hyperon polarization in  $\nu_\mu$  charged current interactions in the NOMAD experiment,” *Nuclear Physics A*, vol. 692, no. 1–2, pp. 73–80, 2001.
- [25] P. Astier, D. Autiero, A. Baldisseri et al., “Measurement of the  $\Lambda$  polarization in  $\nu_\mu$  charged current interactions in the NOMAD experiment,” *Nuclear Physics B*, vol. 605, no. 1–3, pp. 3–14, 2001.
- [26] S. Willocq, P. Marage, M. Aderholz et al., “Neutral strange particle production in antineutrino-neon charged current interactions,” *Zeitschrift für Physik C*, vol. 53, no. 2, pp. 207–217, 1992.
- [27] G. T. Jones, R. W. L. Jones, B. W. Kennedy et al., “Neutral strange particle production in neutrino and antineutrino charged current interactions on protons,” *Zeitschrift für Physik C*, vol. 57, no. 2, pp. 197–209, 1993.
- [28] D. DeProspero, M. Kalelkar, M. Aderholz et al., “Neutral strange particle production in neutrino and antineutrino charged-current interactions on neon,” *Physical Review D*, vol. 50, no. 11, pp. 6691–6703, 1994.
- [29] O. Samoylov, R. Petti, P. Astier et al., “Search for eV (pseudo) scalar penetrating particles in the SPS neutrino beam,” *Physics Letters B*, vol. 479, no. 4, pp. 371–380, 2000.
- [30] G. P. Zeller, K. S. McFarland, T. Adams et al., “Precise determination of electroweak parameters in neutrino-nucleon scattering,” *Physical Review Letters*, vol. 88, no. 9, article 091802, 4 pages, 2002.
- [31] H. Abramowicz, J. G. H. de Groot, J. Knobloch et al., “Experimental study of opposite-sign dimuons produced in neutrino and antineutrino interactions,” *Zeitschrift für Physik C*, vol. 15, no. 1, pp. 19–31, 1982.
- [32] P. Vilain, G. Wilquet, R. Beyer et al., “Leading-order QCD analysis of neutrino-induced dimuon events,” *The European Physical Journal C*, vol. 11, no. 1, pp. 19–34, 1999.
- [33] P. Astier, D. Autiero, A. Baldisseri et al., “Neutrino production of opposite sign dimuons in the NOMAD experiment,” *Physics Letters B*, vol. 486, no. 1–2, pp. 35–48, 2000.
- [34] A. O. Bazarko, C. G. Arroyo, K. T. Bachmann et al., “Determination of the strange quark content of the nucleon from a next-to-leading-order QCD analysis of neutrino charm production,” *Zeitschrift für Physik C*, vol. 65, no. 2, pp. 189–198, 1995.

- [35] D. Mason, P. Spentzouris, J. Conrad et al., “Measurement of the nucleon strange-antistrange asymmetry at next-to-leading order in QCD from NuTeV dimuon data,” *Physical Review Letters*, vol. 99, no. 19, Article ID 192001, 4 pages, 2007.
- [36] A. Kayis-Topaksu, R. Tsenov, P. Annis et al., “Leading order analysis of neutrino induced dimuon events in the CHORUS experiment,” *Nuclear Physics B*, vol. 798, no. 1-2, pp. 1–16, 2008.
- [37] N. Ushida, T. Kondob, S. Tasaka et al., “Cross sections for neutrino production of charmed particles,” *Physics Letters B*, vol. 206, no. 2, pp. 375–379, 1998.
- [38] P. Astier, D. Autiero, A. Baldisseri et al., “Inclusive production of  $\rho^0(770)$ ,  $f_0(980)$  and  $f_2(1270)$  mesons in  $\nu_\mu$  charged current interactions,” *Nuclear Physics B*, vol. 601, no. 1-2, pp. 3–23, 2001.
- [39] P. Astier, D. Autiero, A. Baldisseri et al., “Bose–Einstein correlations in charged current muon–neutrino interactions in the NOMAD experiment at CERN,” *Nuclear Physics B*, vol. 686, pp. 3–28, 2004.
- [40] Q. K. Wu, S. R. Mishra, A. Godley et al., “A precise measurement of the muon neutrino-nucleon inclusive charged current cross section off an isoscalar target in the energy range  $2.5 < E_\nu < 40$  GeV by NOMAD,” *Physics Letters B*, vol. 660, no. 1-2, pp. 19–25, 2008.
- [41] V. Lyubushkin, B. Popov, J. J. Kim et al., “A study of quasi-elastic muon neutrino and antineutrino scattering in the NOMAD experiment,” *The European Physical Journal C*, vol. 63, no. 3, pp. 355–381, 2009.
- [42] C. T. Kullenberg, S. R. Mishras, M. B. Seaton et al., “A measurement of coherent neutral pion production in neutrino neutral current interactions in the NOMAD experiment,” *Physics Letters B*, vol. 682, no. 2, pp. 177–184, 2009.
- [43] C. T. Kullenberg, G. Bassompierre, J.M. Gaillard et al., “A search for single photon events in neutrino interactions,” *Physics Letters*, vol. B706, no. 4-5, pp. 268–275, 2012.
- [44] P. Astier, D. Autiero, A. Baldisseri et al., “A study of backward going  $p$  and  $\bar{\pi}$  in the  $\nu_\mu CC$  interactions with the NOMAD detector,” *Nuclear Physics B*, vol. 609, no. 3, pp. 255–279, 2001.
- [45] J. Altegoer, P. Astier, D. Autiero et al., “Search for a new gauge boson in  $\pi^0$  decays,” *Physics Letters B*, vol. 428, pp. 197–205, 1998.
- [46] P. Astier, D. Autiero, A. Baldisseri et al., “Search for eV (pseudo)scalar penetrating particles in the SPS neutrino beam,” *Physics Letters B*, vol. 479, no. 4, pp. 371–380, 2000.
- [47] P. Astier, D. Autiero, A. Baldisseri et al., “Search for heavy neutrinos mixing with tau neutrinos,” *Physics Letters*, vol. B506, no. 1-2, pp. 27–38, 2001.
- [48] S. V. Belikov, A. P. Bygorsky, L. A. Klimenko et al., “Quasi-elastic neutrino and antineutrino scattering: total cross sections, axial form factor,” *Zeitschrift für Physik A*, vol. 320, no. 4, pp. 625–633, 1985.
- [49] H. J. Grabosch et al., *Soviet Journal of Nuclear Physics*, vol. 47, p. 1032, 1988.
- [50] J. Brunner et al., “Zeitschrift für Physik A,” vol. 45, p. 551, 1990.
- [51] G. Bernardi, G. Carugno, J. Chauveau et al., “Search for heavy neutrino decay,” *Physics Letters B*, vol. 166, no. 4, pp. 479–483, 1986.
- [52] G. Bernardi, G. Carugno, J. Chauveau et al., “Further limits on heavy neutrino couplings,” *Physics Letters B*, vol. 203, no. 3, pp. 332–334, 1988.



**Hindawi**

Submit your manuscripts at  
<http://www.hindawi.com>

